RSC Advances

Bubble morphological evolution and surface defects formation mechanism in the microcellular foam injection molding process

Journal:	*RSC Advances*
Manuscript ID:	RA-ART-04-2015-007512.R1
Article Type:	Paper
Date Submitted by the Author:	27-Jul-2015

Complete List of Authors:	zhang, lei; Shandong University, Key Laboratory for Liquid-Solid Structural Evolution and Processing of Materials (Ministry of Education) Zhao, Guoqun; Shandong University, Key Laboratory for Liquid-Solid Structural Evolution and Processing of Materials (Ministry of Education) Dong, Guiwei; Shandong University, Key Laboratory for Liquid-Solid Structural Evolution and Processing of Materials (Ministry of Education) Li, Shuai; Shandong University, Key Laboratory for Liquid-Solid Structural Evolution and Processing of Materials (Ministry of Education) Wang, Guilong; Shandong University, Key Laboratory for Liquid-Solid Structural Evolution and Processing of Materials (Ministry of Education)

Bubble morphological evolution and surface defects formation mechanism in the microcellular foam injection molding process

Lei Zhang, Guoqun Zhao*, Guiwei Dong, Shuai Li, Guilong Wang

Key Laboratory for Liquid-Solid Structural Evolution and Processing of Materials (Ministry of Education), Shandong University, Jinan, Shandong 250061, PR China

Abstract

The filling stage of the Microcellular Foam Injection Molding (MFIM) process belongs to a kind of three phase flow process of polymer melt, super critical fluid (SCF) and air. It not only includes the nucleation and growth of spherical bubbles, but also the morphological evolution of the bubbles, such as deformation, burst, vanishing, etc. There are usually silver marks, spiral lines, pits and other defects on the product surface. In order to effectively control the surface quality, it is significant to reveal the morphological evolution law of bubbles and the formation mechanism of surface defects in the filling stage of MFIM. This paper established an incompressible, non-isothermal, and unsteady three-dimensional mathematical model of multiphase flow. A new setting method of boundary conditions with the exhaust function on the mold cavity walls was proposed. The problem of temperature solution divergence on the interface between two phases with high viscosity ratio was solved through the coupling algorithm of energy equation and PIMPLE loop. The tracking accuracy of micron grade bubbles interface in macroscopic scale flow field was improved though Adaptive Meshing Refining (AMR) technique. Based on the above mathematical model, the influence law of temperature field and velocity field on the bubble morphological evolution in the thickness cross-section of the injection flow field was obtained. The deformation, burst and vanishing process of bubbles with different initial sizes and locations in the shear and fountain flow field was predicted. Combined with the short shot experiment, the formation mechanism of pits, silver marks and collapses on the product surface manufactured by MFIM was also revealed.

Key words: Microcellular Foam Injection Molding, Bubbles morphological evolution, Multiphase flow model, Surface defects.

* Corresponding author:

Guoqun Zhao, Key Laboratory for Liquid-Solid Structural Evolution and Processing of Materials (Ministry of Education), Shandong University, Jinan, Shandong 250061, PR China.

Tel. +86-531-88393238, Fax. +86-531-88392811, Email: zhaogq@sdu.edu.cn

1、Introduction

Microcellular Foam Injection Molding (MFIM) process is a polymer molding process producing plastic parts with micron level bubbles inside, in which thermoplastic polymer is used as matrix and Super Critical Fluid (SCF) as the physical foaming agent[1-3]. This technology conforms to the development trend of light-weight and environment protection. It has the superiority in material saving, energy conservation, dimensional accuracy of product, short molding cycle and so on. A host of attentions to the MFIM process have been poured in automobile, electric appliance, communication equipment, biological tissue engineering[4-5] and other fields.

Compared with the batch foaming process, the bubble evolution process of MFIM is more complicated. From the previous research[6-8], it was found that there are two foaming stages in MFIM. One stage occurs in the filling process, in which the pressure drop between runner and cavity causes the polymer melt foaming. The other stage occurs in cooling process, in which the cooling contraction of polymer melt provides pressure drop for nucleation and growth of foaming agent. The first stage belongs to a dynamic foaming process, but the second stage belongs to a static foaming process. These two foaming stages have different foaming degrees and bubble morphologies for different process parameters, product structures and polymer materials. As a result, versatile pore structures will appear inside MFIM products and complex morphology on the surface. In this way, the process control of MFIM becomes complex and difficult. This two-stage foaming process often causes serious silver marks and swirl marks on the surface of MFIM products. Since these defects have not been solved effectively up till now, the popularization and development of MFIM technology are restricted seriously[9].

In order to eliminate the above defects on the surface of MFIM product, it is necessary to ascertain the morphological evolution law of micron grade bubbles and reveal the forming mechanism of various defects. At present, many hypotheses about the forming mechanism of swirl marks and silver marks have been proposed. Cha and Yoon[10] considered that swirl marks were caused by the trapped gas between mold surface and polymer melt. Pierick et al.[11] thought silver marks were caused by the bubbles at melt surface dragged against a mold wall. According to research results of Andreas et al.[12], due to a sudden pressure drop as shooting polymer melt into mold cavity, polymer melt at the flow front becomes oversaturated with dissolved gas, and consequently bubbles are nucleated at flow front. The nucleated bubbles at flow front are moved to the interface between polymer melt and cavity wall, and shows pronounced silver and swirl marks on the surface of the final part. Chen et al.[13, 14] also believed that the appearance of silver marks is attributed to the foaming bubbles that are brought to part surface via fountain flow. From the above research, it is concluded that the formation of swirl marks and silver marks on the product surface is closely related to the filling flow field of MFIM. Nevertheless, the above hypotheses have not theoretically revealed the formation mechanism of surface defects under the action of polymer melt flow field. Unfortunately, the existing bubble nucleation theory[15-17] and growth theory[18-23] also cannot account for the evolution law of non-spherical bubble.

Currently, visualization experiments are used as the main way to study the bubble morphological evolution law in the polymer melt flow fluid. Villamizar and Han[24, 25] observed the deformation phenomenon of bubble affected by the surrounding fluid flow by a visual mold with windows on both sides. Mahmoodi et al.[26] found that the bubble migration velocity can transcend the movement velocity of polymer front, and observed the cracking phenomena of bubbles. Wong and Park[27] built a set of experiment simulation device to observe the nucleation, growth and morphological evolution of bubbles in a shear flow. Ahmadzai et al.[28] studied the influence of mold structure and process parameters on bubble rupture in the injection filling stage. With the help of the above mold visualization technology, the evolution process of bubbles in MFIM can be observed directly. It has played an important role in understanding the formation of the internal structure and surface morphology of MFIM parts. However, mold visualization technology has some obvious deficiencies. As we all know, the size of the bubble in a MFIM part reaches to the micron level, and the distance of bubble migration belongs to the centimeter level. The scale difference makes it difficult for mold visualization technology to simultaneously finish clear capture of bubble shape and whole process tracking of bubble displacement. Furthermore, due to the constraints of transparency of polymer material, the shape of

visual mold and the size of observing window, it is difficult to acquire the whole morphological evolution process in MFIM with the mold visualization technology.

Compared with the above mold visualization method, the numerical simulation provides an effective method to study the morphological evolution of bubbles in MFIM, which is not restricted by polymer material, mold shape and can simultaneously capture bubble shape and track the whole process of bubble displacement. Up to now, several interface-tracking methods (e.g., Level Set Method[29, 34], diffusion-interface model[31], Volume of Fluid Method[35, 36], Lattice Boltzmann Method[37]) and discrete methods (Finite Element Method[29], Finite Volume Method[30, 32], Finite Difference Method[32], Boundary Integral Method[30, 33]) can be used to describe the morphological evolution of the interface between two kinds of fluid. With these numerical simulation methods, a wide variety of mathematical models have been established to simulate the deformation of bubble[29, 32, 36, 37] or droplet[30-35] in simple shear flow. And most of the simulation results[29-31, 33, 35-37] is in agreement with the experimental observations. However, the actual melt flow field in injection molding process is not a simple shear flow field, but a complex flow field coupled by the nonlinear shear flow, the fountain flow and the complex 3D flow field geometry. Furthermore, the aforementioned researches did not considered the influence of inhomogeneous temperature field and shear thinning phenomenon on the fluid viscosity. Up till now, the mathematical modeling and the numerical simulation of bubbles morphological evolution in MFIM flow field have not been carried out yet.

In order to perform numerical simulation of the bubble morphological evolution in the filling process of MFIM, this paper established an incompressible, unsteady, non-isothermal 3D mathematical model of multiphase flow in MFIM process, where the interfacial tension model of SCF/polymer proposed by Park et al.[38] and SCF-concentration-updated Cross-Carreau model proposed by Lee and Park[39] were used to respectively calculate interface tension and melt viscosity. The Navier-Stokes equation with inertia item was used to solve the velocity field and pressure field, and the VOF with a compression item was adopted to track the interface between arbitrary two phases. In order to solve the above model accurately, a new set of boundary conditions of gas filtration on the mold cavity wall was proposed. To solve the divergence problem of temperature field on the interface between two phases with large viscosity ratio, the energy equation was introduced into the PIMPLE algorithm which is usually used to solve the velocity and pressure field, and the coupling algorithm of velocity, pressure and temperature was finally established. The accurate tracking of micron level bubble interface in the large scale flow field was realized by adopting the Adaptive Mesh Refining (AMR) technology[40] based on field variables distribution. Based on the above established model, this paper obtained the influence law of temperature field and velocity field on the bubble morphological evolution in the thickness cross-section of the melt flow field of MFIM process. The deformation, burst and vanishing of bubbles with different initial sizes or locations in the shear and fountain flow field were predicted. The related short shot experiments of MFIM were performed. The bubble morphologies and surface defects were observed by using SEM. Based on the numerical and experimental results, the formation mechanism of pits, silver marks and collapses on product surface molded by MFIM was finally revealed.

2、Mathematical Model and Calculation Method

2.1 Governing Equations

The mathematical model in this paper is established to research the bubble deformation stage after the nucleation and growth stage in the MFIM process. Considering the practical fluid state and calculation amount, we assume that: 1) polymer melt, air and SCF are all incompressible materials, 2) there is no chemical reaction and phase transition in the system, 3) the flow type is laminar, 4) the force of gravity is ignored. According to the above assumption, the conservation of mass, momentum and energy was given as follow.

1、 Mass equation is expressed as

$$\nabla \cdot U = 0 \tag{1}$$

Where U is the velocity field and $\nabla\cdot$ is the divergence operator.

2、 Momentum equation is expressed as

$$\frac{\partial(\rho U)}{\partial t}+\nabla\cdot(\rho UU)=\nabla\cdot T+\rho f_b \tag{2}$$

where ρ is the density, T is the stress tensor, f_b is the interfacial tension and t is time. According to the generalized Newton's laws of internal friction, T can be expressed as

$$T=-\left(P+\frac{2}{3}\mu\nabla\cdot U\right)I+2\mu\varepsilon \tag{3}$$

$$\varepsilon=\frac{1}{2}\left[\nabla U+(\nabla U)^{\mathrm{T}}\right] \tag{4}$$

where P is the pressure field, μ and ε are the kinematic viscosity and the strain rate tensor of the mixed system, respectively, I is the unit tensor. By substituting equation (1) and (3) into (2), and the following momentum equation is obtained.

$$\frac{\partial(\rho U)}{\partial t}+\nabla\cdot(\rho UU)=-\nabla p+\rho f_b+\nabla\cdot\mu\left[\nabla U+(\nabla U)^{\mathrm{T}}\right] \tag{5}$$

3、 Energy equation is expressed as

$$\frac{\partial(\rho C_p\,\mathrm{T})}{\partial t}+\nabla\cdot\left(\rho UC_p\,\mathrm{T}\right)=\nabla\cdot\left(k\nabla\,\mathrm{T}\right)+\mu\dot{\gamma}^2 \tag{6}$$

where C_p and k are the isobaric heat capacity and the heat conductivity of the mixed system, respectively, $\dot{\gamma}$ is the modulus of strain rate tensor ε and its expression is as follow:

$$\dot{\gamma}=\left|\varepsilon(U)\right|=\sqrt{2\varepsilon(U):\varepsilon(U)} \tag{7}$$

Physical property Φ in the interface between arbitrary two phases can be solved by arithmetic mean of physical properties Φ_i of each phase and expressed as

$$\Phi=\sum_{1}^{n}\alpha_i\Phi_i,(\Phi=C_p,k,\rho,\mu) \tag{8}$$

where i means the ith fluid, α_i is the phase fraction of fluid i in the FVM mesh element of the multiphase interface, and n means the number of phase in the mesh element.

2.2 Interface Tracking Method

In order to study the evolution of the interface in the mixed system composed of polymer melt, SCF and air, this paper indirectly determined the transient location of multi-phase interface by polymer melt phase fraction $\alpha_{polymer}$, SCF phase fraction α_{SCF} and air phase fraction α_{air} in the mesh, where the phase fraction of each phase was solved by using the VOF method with a compression item proposed by Weller[41] as follow.

$$\frac{\partial \alpha_i}{\partial t} + \nabla\cdot\left(U\alpha_i\right) + \nabla\cdot\left[U_r\alpha_i\left(1-\alpha_i\right)\right] = 0 \tag{9}$$

where $\nabla\cdot\left[U_r\alpha_i\left(1-\alpha_i\right)\right]$ is the compression item, and the phase fraction α_i of the fluid i in a mesh element can be regarded as

$$\alpha\left(i,x,y,z,t\right) = \begin{cases} 1, \text{ for the point } \left(x,y,z,t\right) \text{ inside fluid } i \\ 0, \text{ for the point } \left(x,y,z,t\right) \text{ outside fluid } i \\ 0 < \alpha < 1, \text{ for the point } \left(x,y,z,t\right) \text{ inside the interface area} \end{cases}$$

It should be pointed out that this method is a tracking method defining the interface with a limited thickness[42]. Although an artificial error is inevitably introduced into the fusion and failure process of the interface, in comparison with zero interface thickness methods such as Front-tracking method[43] and moving mesh method[40], this method is still a kind of appropriate interface tracking method in dealing with the bubble morphological evolution in the complex 3D fountain flow field of mixed system with large viscosity ratio[44].

2.3 Interfacial Tension

In the mold cavity, there are three pairs of interface (polymer/SCF, polymer/air and SCF/air) between different fluids. Among these interfaces, the interfacial tensions of polymer/air and SCF/air are much smaller than that of polymer/SCF because the curvature difference. Furthermore, they will not influence the bubble morphology directly. In the way, the interfacial tensions of polymer/air and SCF/air are ignored in this paper. In order to accurately describe the bubble morphology in the shear and fountain flow field, the interfacial tension between SCF and polymer melt is translated into volume force form by using the following Continuum Surface Force (CSF) model proposed by Brackbill et al.[45].

$$f_b = \sigma\kappa\nabla\alpha \tag{10}$$

where σ is the surface tension coefficient between polymer melt and SCF, κ is the curvature of the free interface and defined as

$$\kappa = -\nabla\cdot\left(\frac{\nabla\alpha}{\left|\nabla\alpha\right|}\right) \tag{11}$$

The above surface tension coefficient σ is a function of temperature and pressure. It can be solved by a second order linear regression equation form[38] expressed as follow:

$$\sigma = D_0 - D_T T - D_P P + D_{TP} TP \tag{12}$$

where the equation coefficients D_0, D_T, D_P, D_{TP} are associated with the material properties of polymer/SCF mixed system and can be obtained by using pendant drop method in SCF with high temperature and pressure

2.4 Viscosity Model

In the mathematic model established in this paper, the viscosity of SCF and air is respectively assumed as constant. The viscosity of the polymer melt is calculated through the viscosity model in the consideration of the SCF plasticizing effect on polymer melt[46, 47]. At present, the plasticizing mechanism is explained through free volume theory of polymer[48]. Lee and Park[39] proposed the following Cross-Carreau viscosity model of homogeneous system of polystyrene/supercritical CO_2 (PS/$SCCO_2$) by introducing the concentration of $SCCO_2$ and pressure into the Arrhenius

equation of zero shear viscosity.

$$\eta = \frac{\eta_0}{\left[1+\left(\frac{\eta_0\dot{\gamma}}{\tau}\right)^a\right]^{\frac{(1-m)}{a}}} \tag{13}$$

$$\eta_0 = A\exp\left(\frac{b}{T-T_r}+\beta P+\psi C\right) \tag{14}$$

where η_0 and η denote the zero shear viscosity and dynamic viscosity, respectively. C is the mass concentration fraction of SCF. A, b, β, ψ, T_r, τ, a and m are the model parameters related to the material, which can be obtained by using online measurement in a foaming extruder with GCP control equipment[39, 49].

The kinematic viscosity μ in the momentum equation can be calculated by

$$\mu = \frac{\eta}{\rho} \tag{14}$$

2.5 Boundary Condition

The solution of the above mathematical model needs a set of appropriate boundary conditions. Hetu et al.[50] proposed a kind of hybrid exhaust boundary conditions based on the two phase flow model, in which the phase fraction of polymer was denoted by α with the value ranging from 0 to 1 and the critical phase fraction of polymer was denoted by α_c. When $\alpha \geq \alpha_c$, the hybrid boundary condition is expressed as no-slip boundary condition. When $\alpha < \alpha_c$, it is expressed as the exhaust boundary condition. The value of α_c is the key to control the exhaust. However, it is hard to meanwhile ensure the cavity filling of polymer melt and emptying of air with just one parameter α_c. Usually, the volume fraction of lost polymer in the boundary mesh may be up to 20%-50%.

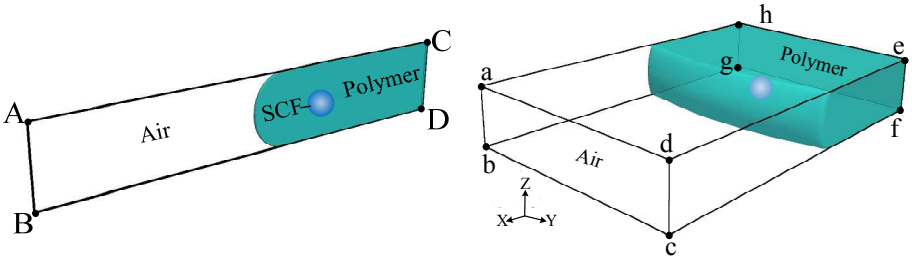

(a) (b)

Figure 1. Diagram of boundary conditions of 2D and 3D model of MIFM filling stage. (a) 2D model, (b) 3D model

In order to solve the above problems, this paper proposed a set of new hybrid exhaust boundary condition of the multiphase model and its transformation criterion. In the consideration of the practical structure characteristics of injection mold, two kinds of exhaust boundary conditions with different transformation criterions are put forward. One is the boundary condition of cavity profile, the other one is the boundary condition in the filling end of cavity.

Figure 1 shows the diagram of boundary conditions for 2D and 3D model of MIFM filling process. Among these boundary conditions, Γ_{wall} belongs to the no-slip type, $\Gamma_{profile}$ and Γ_{vent} belong to the hybrid type for realizing the

exhaust function of mold cavity. Table 1 gives the complete boundary conditions in this paper.

Table 1 Application method of the complete boundary conditions for multiphase flow model of MIFM filling process

Boundary	2D model	3Dmodel	Boundary condition
Γ_{inlet}	Line CD	Face efgh	$\{T = T_{inlet}, U = U_{inlet}, \nabla P = 0\}$
Γ_{wall}	Line AC Line BD	Face adeh Face bcfg	$\{T = T_{wall}, U = 0, \nabla P = 0\}$
$\Gamma_{profile}$		Face abhg Face cdef	$\Gamma_{profile-air}\{T = T_{profile}, \nabla U = 0, P = P_0\}$ $\Gamma_{profile-polymer}\{T = T_{profile}, U = 0, \nabla P = 0\}$
Γ_{vent}	Line AB	Face abcd	$\Gamma_{vent-air}\{T = T_{vent}, \nabla U = 0, P = P_0\}$ $\Gamma_{vent-polymer}\{T = T_{vent}, U = 0, \nabla P = 0\}$
Γ_{empty}	Face ABCD		*Empty*

For the boundary condition of the cavity profile $\Gamma_{profile}$, when $\alpha_{polymer} < c_1 \bigcap \alpha_{SCF} < c_2 \bigcap \alpha_{air} > c_3$, the condition of $\Gamma_{profile-air}\{T = T_{profile}, \nabla U = 0, P = P_0\}$ is used, when $\alpha_{polymer} \geq c_1 \bigcup \alpha_{SCF} \geq c_2 \bigcup \alpha_{air} \leq c_3$, the condition of $\Gamma_{profile-polymer}\{T = T_{profile}, U = 0, \nabla P = 0\}$ is used. For the boundary condition of intensifying venting Γ_{vent}, when $\alpha_{polymer} < C_1 \bigcap \alpha_{SCF} < C_2 \bigcap \alpha_{air} > C_3$, the condition of $\Gamma_{vent-air}\{T = T_{vent}, \nabla U = 0, P = P_0\}$ is used, when $\alpha_{polymer} \geq C_1 \bigcup \alpha_{SCF} \geq C_2 \bigcup \alpha_{air} \leq C_3$, the condition of $\Gamma_{vent-polymer}\{T = T_{vent}, U = 0, \nabla P = 0\}$ is used.

$c_1, c_2, c_3, C_1, C_2, C_3$ in the above conditions are the judgment parameters. Considering the same flow behaviors of SCF and polymer melt on $\Gamma_{profile}$ and Γ_{vent}, c_1, c_2, C_1, C_2 are suggested to be defined in range of 0.001~0.01 to effective control the polymer overflow no more than 1% on the boundary mesh. c_3, C_3 should be defined to ensure the free-flowing exhaust and avoid numerical instability. In this paper, we assigned 0.001, 0.001, 0.9, 0.01, 0.01 and 0.8 to $c_1, c_2, c_3, C_1, C_2, C_3$, respectively.

In the consideration of the coupling relationship of velocity and pressure in the momentum equation, this paper defined the boundary condition of the velocity and pressure of each physical boundary as different types such as Dirichlet or Neumann boundary condition.

2.6 Calculation Methods and Procedures

In this paper, coupled problem of velocity field and pressure field in the momentum equation was solved by using the PIMPLE algorithm[51, 52]. Unfortunately, this research involves the solution of energy conservation equation on the interface between two phases with large viscosity ratio. If traditional PIMPLE algorithm is used as solution method, the divergence of temperature field with unreasonable fluid flow is easily caused, as shown in figure 2(a). To solve this

problem, this paper introduced the energy equation into the PIMPLE algorithm and increased the coupling of temperature field, velocity field and pressure field. Consequently, a more reasonable temperature field distribution is acquired by the above method, as shown in figure 2(b).

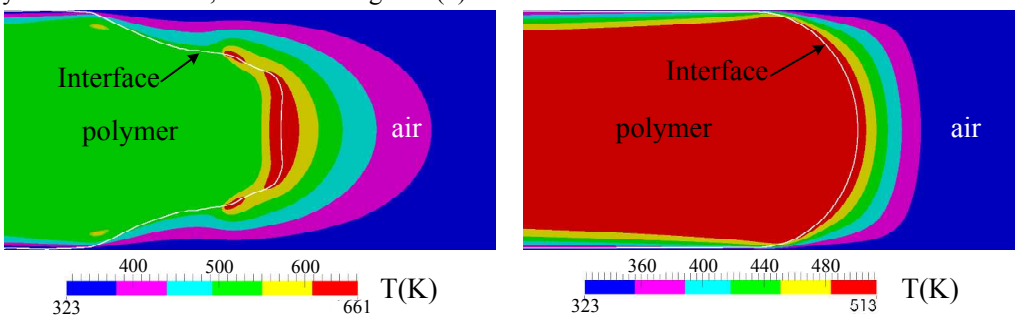

(a) (b)

Figure 2 Comparison of temperature results on the interface between polymer and air acquired by the traditional algorithm and the algorithm of this paper. (a) Result of traditional PIMPLE algorithm, (b) result of algorithm of this paper

Furthermore, to obtain more accurate bubble morphological characteristics, the mesh size in interface area can not be over 1% of bubble diameter. If one wants to calculate of macroscopic field quantities in MFIM and precisely capture the bubble interface with micron level simultaneously, mesh with uniform and small size will lead to huge computational overhead due to the large scale difference between the bubble and the mold cavity. To solve this problem, AMR technique[53, 54] is used in this research. In each time step of calculation process, the mesh surrounding the interface is automatically refined according to the distribution state of phase. Figure 3 shows the mesh division result through AMR, and the mesh on the flow front and polymer surface was deleted for clarity. As shown in the figure 3, the mesh on the polymer flow front interface and bubble interface has been refined, and the interfaces between different phases are clear and smooth.

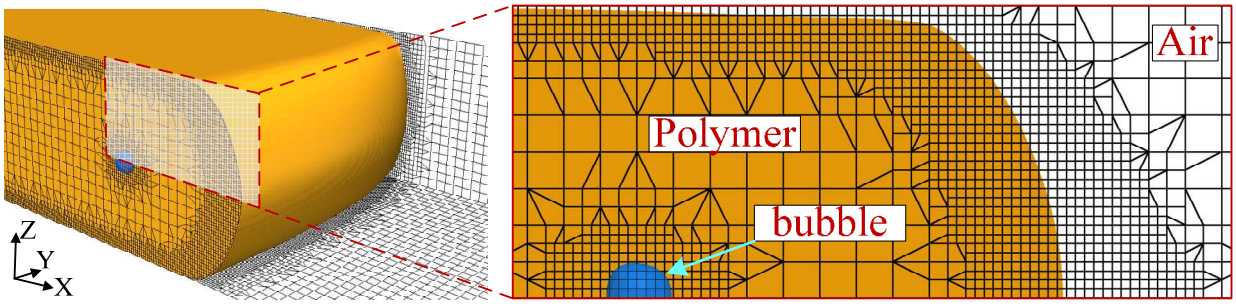

Figure 3 Mesh division result by using AMR technology

In this research, a program based on FVM named as Non-isothermal Multiphase Flow Simulation System (N-MPFS), was developed based on OpenFOAM[51] which is an open source database of computational fluid mechanics. The whole calculation flow chart of this program is shown in figure 4, where figure 4(b) is the PIMPLE loop of the whole flow chart. The calculation method and procedures of this program are stated as fellows.

(1) Generate the initial mesh of calculation model. Input physical parameters, velocity, pressure, phase fraction, temperature of each material. Set the boundary condition parameters and time step control parameters. Start the first time step loop.

(2) Calculate the time step according the Courant number, then calculate the polymer viscosity and mixed material parameters of multiphase flow. Solve the phase fraction equation, and enter into the PIMPLE iteration loop.

(3) The PIMPLE iteration loop includes the inside and outside loops. After solving the velocity and temperature fields in the outside of SIMPLE iteration loop, enter into the inside loop of the PISO iteration to solve the pressure field. Then calculate the flux on the surface of mesh and correct the velocity field. Judge the velocity and pressure fields are converged or not. If converged, break the PISO loop and return to SIMPLE loop. If not, continue the PISO

loop until PISO iteration is converged.

(4) Determine whether the converged results of PISO loop satisfy the convergence criterion of SIMPLE algorithm. If satisfying, break the PIMPLE loop. If not, continue the SIMPLE loop until SIMPLE iteration is converged. According to the converged results, calculate the shear stress tensor, strain rate tensor and viscous dissipation field, and update the mesh by AMR.

(5) Check whether the mold cavity is completely filled or not. If not, the program will enter into the next time step and repeat the above procedures (2)–(4) until the polymer completely fills the mold cavity.

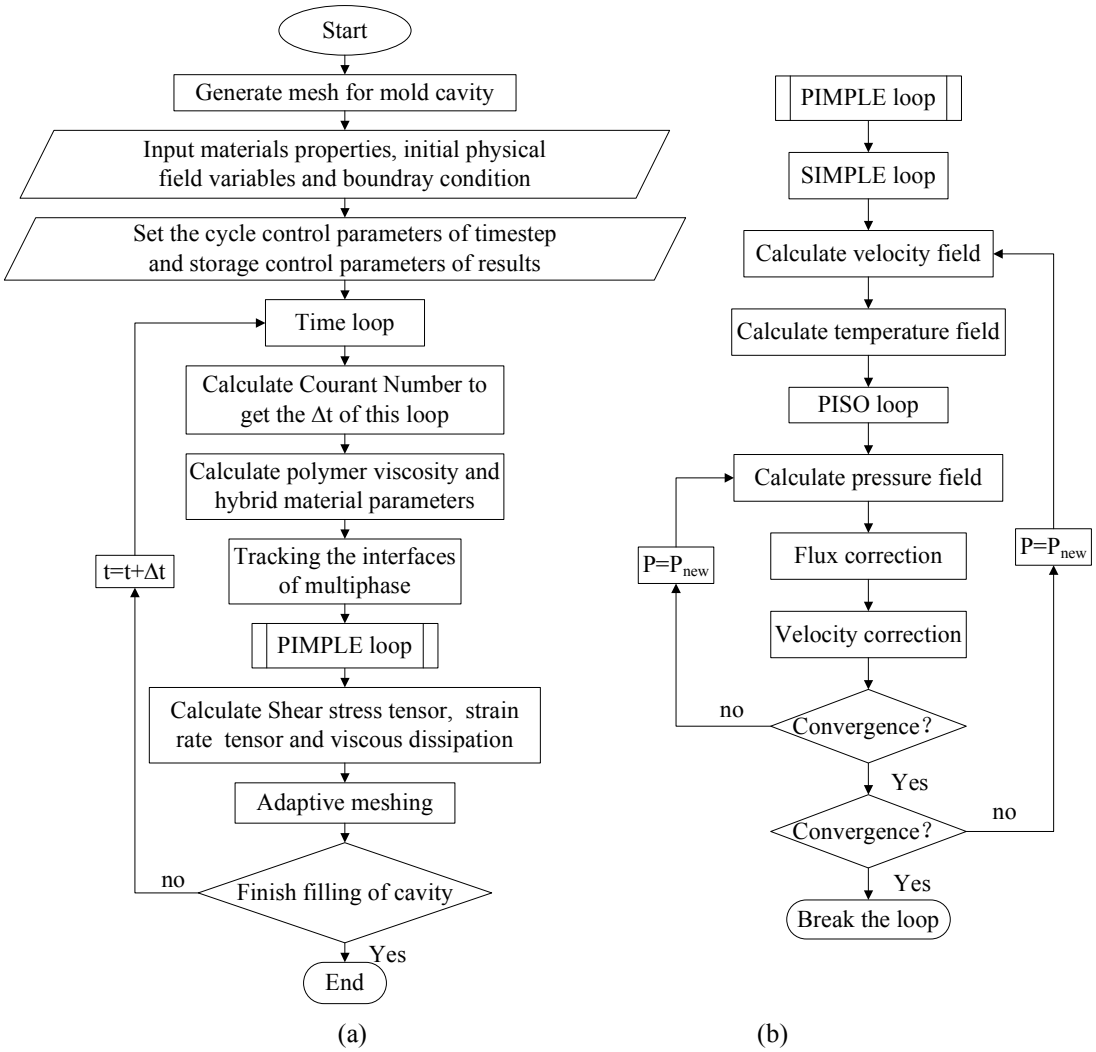

Figure 4 Calculation flow chart of program N-MPFS. (a) whole flow chart, (b) flow chart of PIMPLE loop

3、Model Validation

Compared with the MFIM technology, the deformation law of the bubble in Microcellular Foam Extrusion (MFE) flow field has been revealed more explicitly. Yoo and Han[55, 56] carried out the research of MFE process early, established a set of visualization system of MFE process, and observed the deformation of bubble in a converging extrusion mold, as shown in figure 5. The observed bubble had an initial diameter of 0.1mm and located on the center line of the flow field with a distance of 1.3mm from the outlet. The temperature of polymer melt and mold were all 200°C. Although they used chemical blowing agent (Sodium bicarbonate was used to produce carbon dioxide), same with our mathematical model, the process they researched was also the bubble deformation stage after the bubble growth. In this way, Han's results are appropriate to validate our mathematical model.

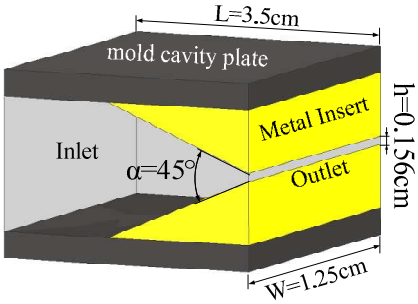

Figure 5 Schematic diagram of the converging die in visualization system built by Han et al.[55]

In the numerical simulation process, the initial filed variables and boundary conditions are kept the same with those in literature[55], and the other model parameters that were not reported in the literature are determined by referencing other literatures. The parameters (D_0, D_T, D_P, D_{TP}) in the interfacial tension model (Eqs.14) are assigned with 38.7032, 0.0559, 0.01, 2.596×10^{-5}, respectively[39], and the parameters (A, b, β, ψ, T_r, τ, a, m) in the polymer viscosity model (Eqs.15, 16) are assigned with 0.8298, 1272K, 6.032×10^{-13}Pa^{-1}, -66.51, 341.1K, 23160Pa, 1.877, 0.265, respectively[39]. The physical parameters of the fluid for the model validation are presented in table 2.

Table 2 Physical parameters of the fluids used for the model validation

Materials	Density ($kg\cdot m^{-3}$)	Specific isobar heat capacity ($J\cdot kg^{-1}\cdot K^{-1}$)	Heat conductance ($W\cdot m^{-1}\cdot K^{-1}$)	Kinematic viscosity ($m^2\cdot s^{-1}$)
PS	954.17	2100	0.15	Eqs.15, 16
CO_2	11.29	1011	0.03157	2×10^{-6}

Figure 6 compared the experimental observation and simulation results of bubble deformation process in the converging die. Alphabet a, b, c, d on the horizontal axis in the figure represent the different positions on the neutral plane of the flow field, where alphabet a represents the farthest distance from the mold outlet and alphabet d represents the location nearest the outlet. Vertical coordinates show the bubble shape parameter D [57], which can be calculated by the equation shown in figure 6. The D value of a round bubble equals to 0, and the D value of a tenuous shape of bubble close to 1. The solid black bubbles in the figure are those observed from the Yoo's experiment, and the hollow bubbles in the figure are those obtained from the simulation of this paper.

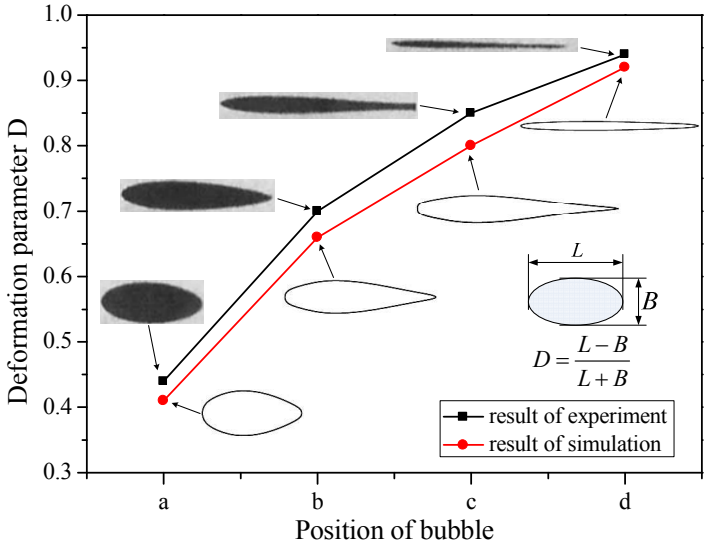

Figure 6 Comparison of experimental observation results and simulation results

After comparing two groups of bubbles shape shown in the figure 6, it can be seen that both the deformation law and the shapes of two groups of bubbles are quite identical in the whole extrusion process. The bubble shape is

gradually changed from egg shape to fusiform shape and then to slender shape with the progress of extrusion process. The D values of bubbles on the four positions obtained from the visual observation are 0.41, 0.66, 0.8 and 0.92, respectively, and the D values of bubbles obtained from the simulation are 0.44, 0.70, 0.85 and 0.94, respectively. Obviously, the two groups of bubble have the similar D value of bubble on each position. The greatest error of D value between two groups of bubble is less than 6.8%. It is manifested that the mathematical model established in this paper is feasible to simulate bubble deformation process in the viscous fluid.

However, the D value obtained from the model established in this paper is slightly lower than the result of visual observation (average 5.1%). This means that the bubble shape of visual observation is slightly more slender than that of simulated result. In practical MFE process, the polymer elasticity in the converging MFE mold will cause the fluid pressure rising near the outlet, and this rising pressure will squeeze the bubble to be increasingly slender. Therefore, the reason of above small error may be caused by ignoring the elasticity of polymer melt in the constitutive model used in the mathematical model

Different from MFE process, the injection molded parts are designed by using the uniform thickness rules. There is rarely converging flow field in the injection mold cavity, and the rising of pressure caused by the polymer elasticity will be inconspicuous. In this way, the mathematic model established in this paper ignoring the influence of polymer elasticity on the bubble shape is feasible to simulate the morphological evolution of bubble in the filling process of MFIM.

4、MFIM Experiment study

In order to further validate the feasibility of the mathematical model established in this paper, clarify the morphological evolution law of bubbles in the MFIM process and reveal the formation mechanism of defects on the surface of the MFIM part, flexural sample (ASTM D790) was chosen to do the MFIM short shot experiment with 40% injection content, as shown in figure 7(b). The research team of authors developed a SCF generator and its measuring conveying system. They were mounted on a MA3200 conventional injection molding machine manufactured by Ningbo Haitian plastic machinery group co., LTD. The shut-off nozzle is provided by Herzog, Switzerland. A specially designed screw with diameter of 60 mm and ratio of length to diameter of 22:1 was installed on the machine. A sample MFIM mold was designed and manufactured. Supercritical N_2 (SCN_2) with the purity of 99.99% was used as the physical foaming agent. High Impact Polystyrene (HIPS, PH-888 G) provided by Zhenjiang Chimei Chemical Industry Co. LTD. was selected as the matrix polymer. The polymer was dried more than 10 hours at 80°C before using. The process parameters for MFIM short shot experiment are shown in table 3.

Table 3 Process parameters of MFIM short shot experiment of flexural sample

Process parameters	Value
Injection delay time (s)	10
Injection rate (mm/s)	10
Injection time (s)	2.5
Melt temperature (°C)	240
Mold temperature (°C)	50
Supercritical fluid level (wt%)	0.3
Cooling time (s)	20
Cooling water temperature (°C)	10

Figure 7 gives the SEM photos on the surface of flexural sample with 40% short shot, where figure 7(a) shows the SEM photo (200×) of the sample surface, figure 7(b) shows the amplified photo of the front-end of flexural sample and figure 7(c) shows the SEM photo (30×) of the front-end of flexural sample. It can clearly distinguish the silver marks (groove), pit defects on the surface and front-end of flexural sample. In figure 7(a), there are a sea of zonal grooves and some pits marked by the dotted line on the surface of flexural sample. In the figure 7(c), there are many the fusiform pits surrounded with the bubble skin on the front-end of polymer. The reasons and mechanism of the formation of these

defects morphology on the sample surface will be revealed in the following section according to the numerical simulation and short shot experiment results. It is worthy to notice here that the geometric and process parameters of the numerical simulation are the same with those of the experiment, but due to the restriction of experimental conditions, it is hard to guarantee consistency of material physical parameters of these two methods, such as viscosity and interfacial tension coefficient.

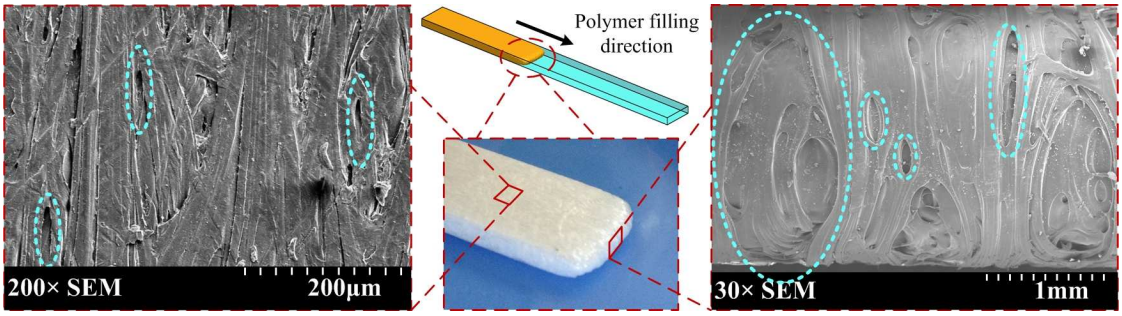

(a) (b) (c)

Figure 7 SEM photos on the surface of flexural sample with 40% short shot. (a) SEM photo (200×) on the sample surface, (b) Amplified photo on the front-end of flexural sample, (c) SEM photo (30×) on the front-end of flexural sample

5、Results and discussion

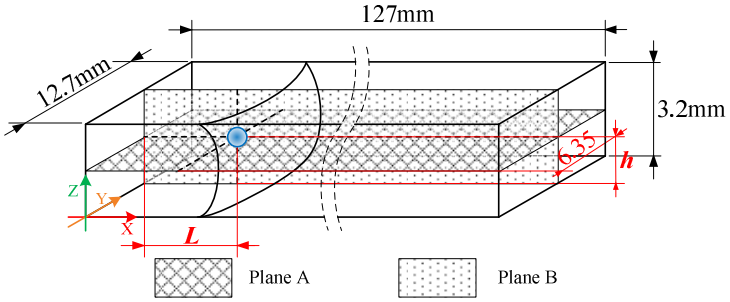

Figure 8 Schematic diagram of the initial state of bubble for simulating morphological evolution in MFIM, where plane A is the central plane of injection flow field on thickness direction (neutral plane), plane B is the central plane of injection flow field on width direction.

Table 4 Numerical simulation scheme of morphological evolution of bubble with different initial diameter and position

Scheme No.	h /mm	L /mm	d /mm
1	1.6	1	0.15
2	1.6	1	0.2
3	1.6	1	0.25
4	1.6	1.5	0.2
5	1.6	0.5	0.2
6	2.4	1	0.15
7	2.4	1	0.2
8	2.4	1	0.25
9	2.0	1	0.2
10	2.8	1	0.2

The morphological evolution of bubble in the flexural sample (ASTM D790) filling stage of MFIM process was simulated by the above mathematical model. The melt filling state of 0.2s in MFIM was defined as the initial state for numerical simulation of bubble morphological evolution. Figure 8 shows the schematic diagram of the initial simulation state. The X direction is the polymer filling direction, Y direction is the cavity width direction, and Z

direction is the cavity thickness direction. All the results of later numerical simulation will use the same coordinate system as figure 8. The initial bubble is spherical with d as the diameter, and the initial coordinate of center of spherical bubble is defined as (L , 6.35, h). Different values of h , L and d are assigned to study the morphological evolution of bubble with different initial diameters and positions in MFIM process, as listed in table 4.

Here, the initial physical variables and boundary conditions refer to the process parameter in the table 3, and the coefficients of the viscosity model and the interfacial tension model are consistent with those in section 3 of this paper. Table 5 lists the fluid physical property parameters needed here.

Table 5 Physical property parameters in simulating bubble morphological evolution in MFIM process

Materials	Density ($kg \cdot m^{-3}$)	Specific isobar heat capacity ($J \cdot kg^{-1} \cdot K^{-1}$)	Heat conductance ($W \cdot m^{-1} \cdot K^{-1}$)	Kinematic viscosity ($m^2 \cdot s^{-1}$)
HIPS	927.68	2100	0.18	Eqs.15, 16
N_2	13.14	1068	0.040	2×10^{-6}
Air	1.078	1008	0.027	1.8×10^{-5}

5.1 Morphological Evolution of bubble on the neutral plane of injection flow field

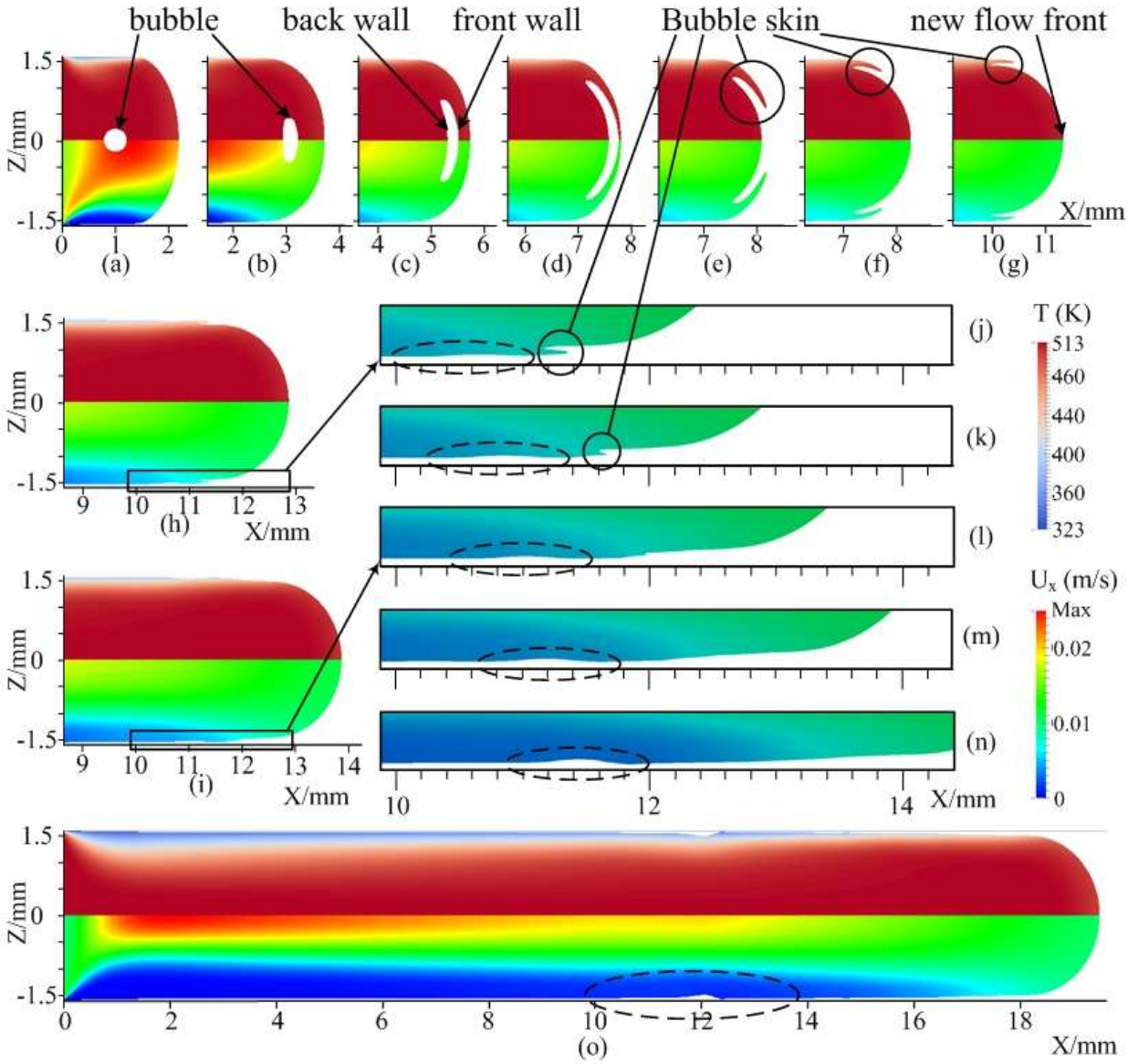

Figure 9 Numerical simulation result of bubble evolution process of scheme 2 in table 4

Figure 9 shows the numerical simulation result of bubble evolution process of scheme 2 (h =1.6mm, L =1mm, d =0.2mm) in table 4. All of the pictures in figure 9 are the sectional view (Y=6.35mm) of 3D result. The upper half of figure 9(a)-(i) and (o) shows the temperature distribution of polymer melt and the bottom half shows the velocity distribution of the polymer melt on the X axis direction. The figure 9(j)-(n) show the magnification of velocity distribution of the polymer melt on the X direction during filling time of 1.05s to 1.3s.

Figure 9(a)-(g) give the deformation and burst process of the bubble, and figure 9(h), (i), and (o) show the formation process of polymer surface defects. The corresponding relation between figure icon, filling time and the maximum melt flow velocity is listed in table 6.

Table 6 Corresponding relations between figure icon, filling time and the maximum melt flow velocity

Figure icon	Time(s)	Max. U_x (m/s)
a	0	0.0161
b	0.15	0.0172
c	0.35	0.0192
d	0.55	0.0206
e	0.6	0.0209
f	0.8	0.022
g	0.9	0.0225
h	1.05	0.0231
i	1.15	0.0235
j	1.05	0.0231
k	1.1	0.0231
l	1.15	0.0231
m	1.2	0.0231
n	1.25	0.0231
o	1.7	0.0252

From figure 9(a) to (c), It can be seen that the bubble shape in the injection flow field changes from circular to elliptical and then crescent. This is because that the trailing melt flows faster than the front melt on the X direction, and there is a velocity gradient on the X direction of injection flow field. The trailing melt will squeeze the bubble and concurrently push it approaching toward the flow front. This phenomenon was also confirmed by the visualization experiment research results of Mahmoodi et al.[23].

Figure 9(d)-(g) give the bubble burst process at the flow forefront. The bubble becomes extremely flattened under the action of fountain flow, and the bubble interface can be divided into front wall and rear wall, as shown in figure 9(c). When the filling time is 0.55s, the front wall of bubble almost fused with the flow front interface, and the bubble is about to burst. After the bubble bursting, the rear wall of bubble becomes the new flow front of filling polymer, as shown in figure 9(e). The bubble skin is formed after the bubble bursts, as shown as solid circle mark in figure 9. The bubble skin is conveyed to the mold surface by fountain flow and continually fuses into the polymer melt with size shrinking, as shown in figure 9(e), (f), and (g). At last, it disappears. The partially enlarged figure 9(j)-(n) shows the disappearing process of the bubble skin.

In addition, from figure 9, it can be also found that a collapse phenomenon behind the bubble skin on the sample surface appears when the bubble skin disappears, as shown as the dotted elliptical mark in figure 9. This collapse phenomenon was also found from the SEM photo of the flexural sample surface molded by the short shot experiment, which is marked by dotted circle in figure 10. This indicates that the collapse phenomenon really exists. The formation reason and condition about the collapse phenomenon will be further analyzed thereinafter.

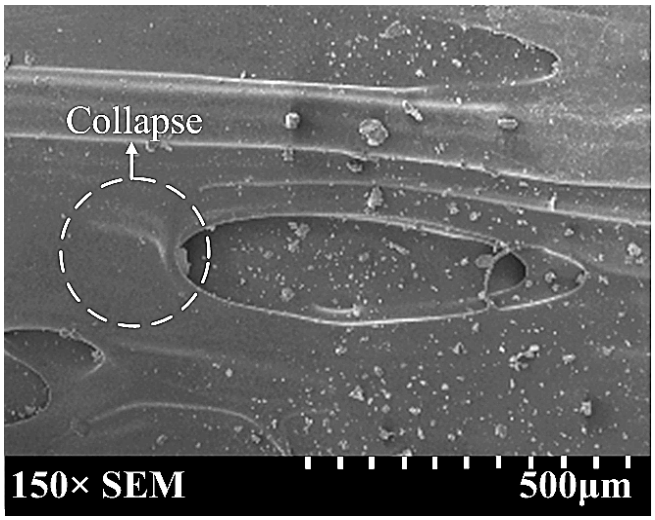

Figure 10 SEM (150×) of flexural sample surface got from the short shot experiment

5.2 Morphological Evolution of bubble with different initial positions and sizes on the neutral plane of injection flow field

In this section, suppose that the initial location of a bubble is located on the thickness center surface of sample (h=1.6mm), and the initial X directional location and diameter of the bubble is changed to study the different morphological evolution of the bubble. Figure 11 shows the bubble morphological evolution of numerical simulation scheme 1, 2 and 3 (h=0.8mm, L=1mm), where the bubble diameters are defined as d_1=0.15mm, d_2=0.2mm, d_3=0.25mm. The three rows of images are corresponding to the simulation scheme 1, 2 and 3, respectively. As shown in figure 11, the shapes of bubbles with three different diameters change from circle to vertical oval and then crescent. The bubble in the first row of images with the smallest size (d_1=0.15mm) produces a bubble skin with relatively small size after burst. The bubble skin atrophies on the flow front interface and vanishes before touching the mold cavity wall, as shown in the 0.8s image of the first row. The second row of images in figure 11 gives the evolution process of the bubble with an initial diameter of 0.2mm. The residual bubble skin after bursting has a larger size, and it vanishes after touching the mold cavity wall under the action of fountain flow, as shown in the 0.95s image of the second row. As the initial diameter of bubble increases continuously, the residual bubble skin after bursting gradually becomes larger, as shown in the third row of figure 11. The bubble skin vanishes after touching the mold cavity wall and sliding a distance along it, as shown in the 1.15s image of the third row.

It can be seen from figure 11 that the bubble skin will completely vanish on the flow front interface when the initial position of small size bubble is located on the neutral plane of flow field. It will not be conveyed to the mold surface by the fountain flow. As a result, it will not cause surface defects on the plastic part. Therefore, not all the burst bubbles will lead to the defect on the surface of the plastic part. But, when the initial position of big size bubble is located on the neutral plane of flow field, the bubble skin will be pushed to the mold cavity surface by the fountain flow and cause the defects on the surface of plastic part. The larger diameter of the bubble is, the more serious defects on the surface of plastic part there will be.

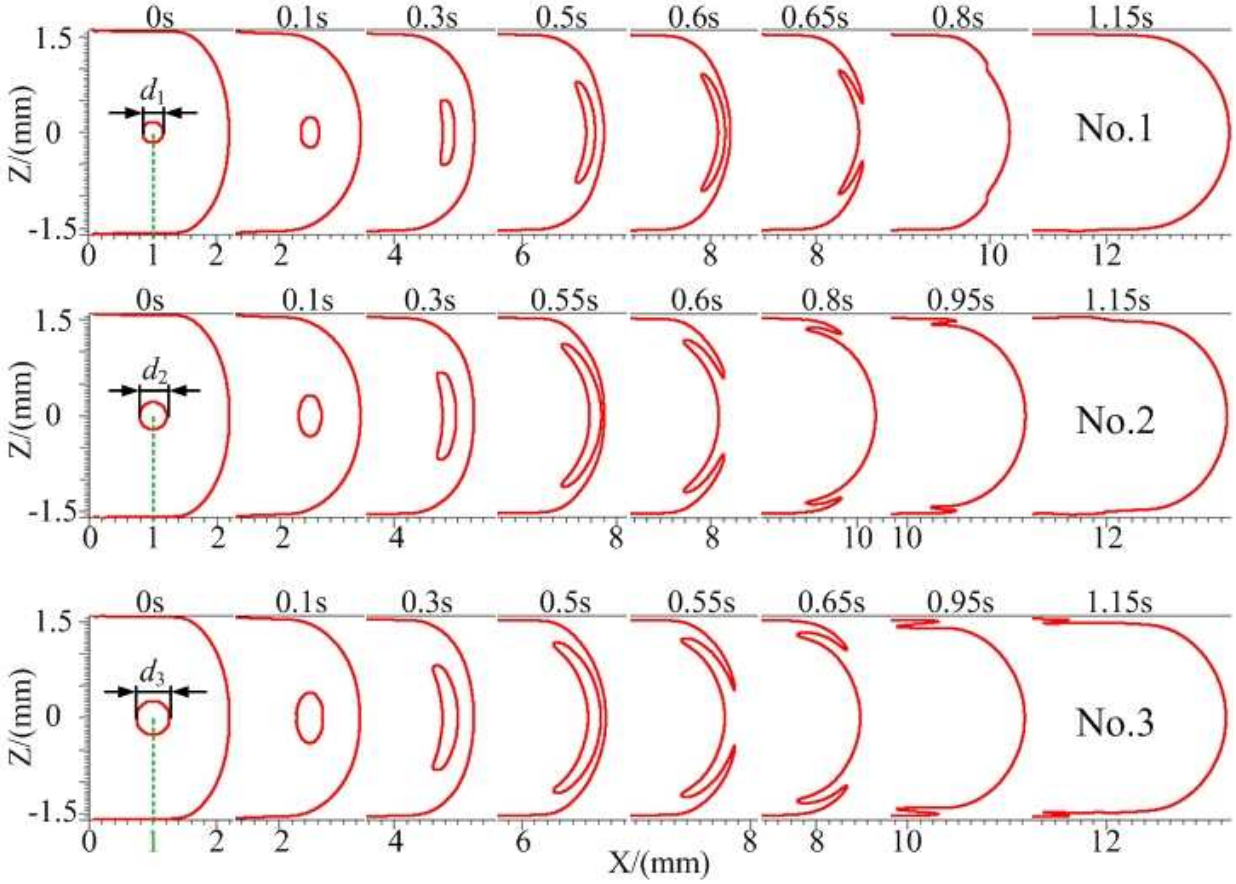

Figure 11 Morphological evolution of bubble in the front part of melt obtained from simulation scheme 1, 2 and 3

In order to further reveal the bubble burst and disappearance process of the bubble skin, this paper also studied the bubble burst process on the flow front interface, and the simulation result is shown in figure 12. Figure 12(a) shows the flow front and the viewing angle of bubble. Figure 12(b) gives a locally amplified area of a pit in the SEM photo in the figure 7(c), and it really reflects the morphology of the pit on the flow front interface. Figure 12(c) shows the simulation result of bubble bursting process on the flow front interface obtained from the simulation scheme 1.

As shown in the 0.6s image of figure 12(c), the bubble shape has changed to oval shape before bursting. Following the polymer continuously filling in the mold cavity, the bubble starts to burst, and the crevasse on the flow front interface exhibits an oval shape. From the images of 0.604s to 0.64s shown in figure 12(c), in this short period of time, the crevasse expanded rapidly. As a result, the size of the crevasse gradually approaches to that of the burst bubble, and the size of bubble skin continuously shrinks and finally evolves into a narrow annulus. When the filling time reaches 0.7s, the bubble skin on the ends of the minor axis of oval disappears completely, and the bubble skin on the ends of the long axis still has a little rest. Compared with the SEM photo of the crevasse morphology shown in figure 12(b), the simulation results are in good agreement with those of experiments. When the filling time reaches 0.8s, the bubble skin disappears completely. Compared with the results of the moment before, the crevasse at this moment has been obviously stretched by the fountain flow on the long axis of bubble. The bubble after bursting forms spindle pit morphology on the flow front interface, as shown in the B-B sectional view in figure 12(c).

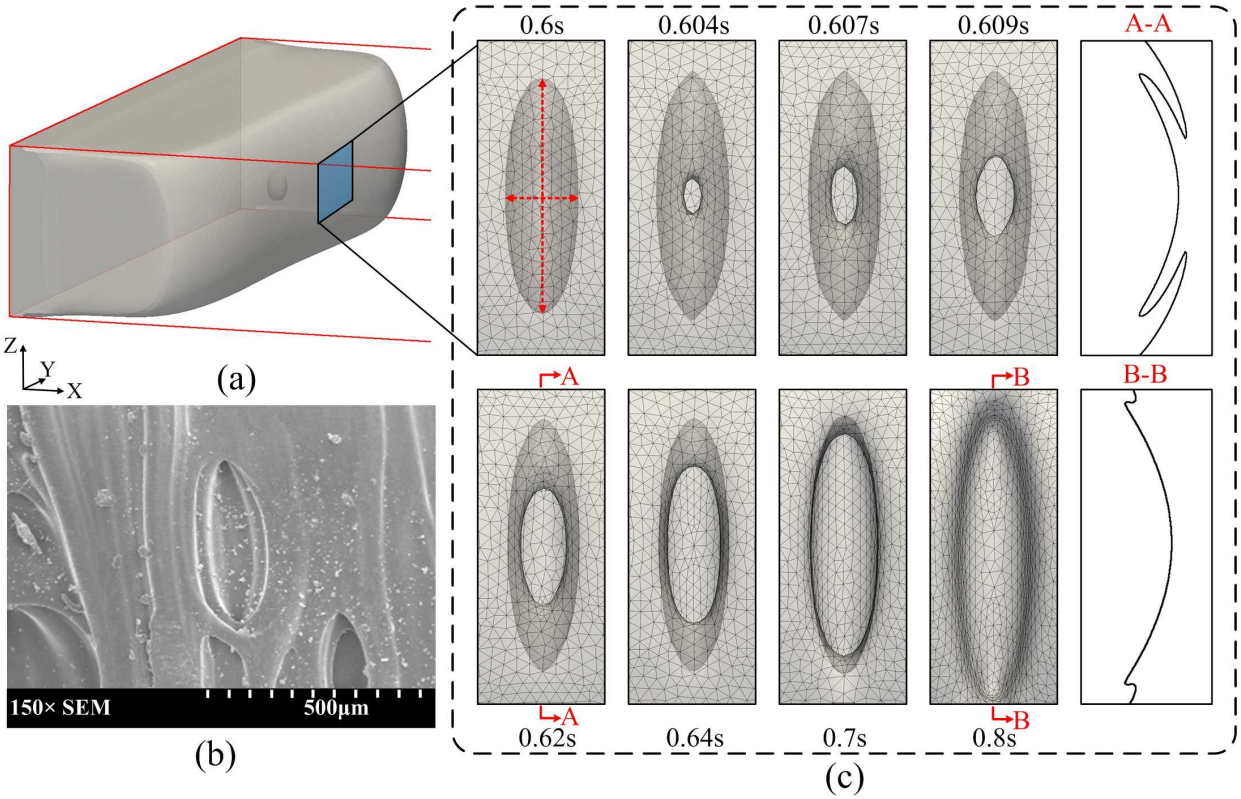

Figure 12 Bubble bursting process on the flow front. (a) flow front and viewing angle of bubble, (b) SEM of the pit, (c) simulation result of bubble bursting process on the flow front interface.

In order to study the morphological evolution law of bubble with different initial positions on the X direction, the simulation scheme 5, 2 and 4 (h=1.6mm, d=0.2mm) were performed. Figure 13 gives the numerical simulation results of there schemes. The three rows of images in figure 13 respectively correspond to the results of simulation scheme 5, 2 and 4, where L_1=0.5mm, L_2=1mm and L_3=1.5mm. Figure 13(a), (b) and (c) respectively show the partially enlarged drawing of the residual bubble skin with three different positions.

From figure 13, it can be seen that the deformation, bursting and disappearing process of bubble with different initial positions are quite different. When the initial position of the bubble is near the inlet of flow field (value of L is the smallest), the simulation results are shown in the first row of image of figure 12. The bubble shape becomes an approximate ellipse with long axis along the X direction in the early deformation stage, as shown in the image of 0.05s in the first row. Then, it changes to an approximate ellipse with long axis along the Z direction, as shown in the image of 0.3s in the first row. Subsequently, it evolves to a crescent shape under the squeezing action of the fountain flow field, as shown in the image of 0.8s in the first row. At last, the bubble burst and its skin is gradually pushed onto the mold cavity wall surface. When the initial position of the bubble is relatively far away from the inlet of flow field (value of L is bigger), the morphology of bubble before bursting is different from that of smaller L, as shown in the second and the third row of image in figure 13. The bubble did not evolve to the approximate ellipse with long axis along the X direction in the early deformation stage, but directly evolved to the approximate ellipse with long axis along the Y direction.

Furthermore, different initial positions of bubble correspond to the different bubble bursting time. The shorter the distance from the initial position of bubble to the flow front interface is, the earlier the bubble bursting time is. At the same time, the bubbles with different initial positions have different skin thicknesses after bursting. The longer the distance from the initial position of bubble to flow front interface is, the thinner the bubble skin thickness after bursting is, as shown as t_1 in figure 13(a), t_2 in figure 13(b) and t_3 in figure 13(c). This is because that the initial bubble with a

longer distance to flow front interface has been subject to a long time of action of fountain flow before its bursting, its shape becomes extremely flat after being fully squeezed and the bubble skin after bursting is relatively thinner.

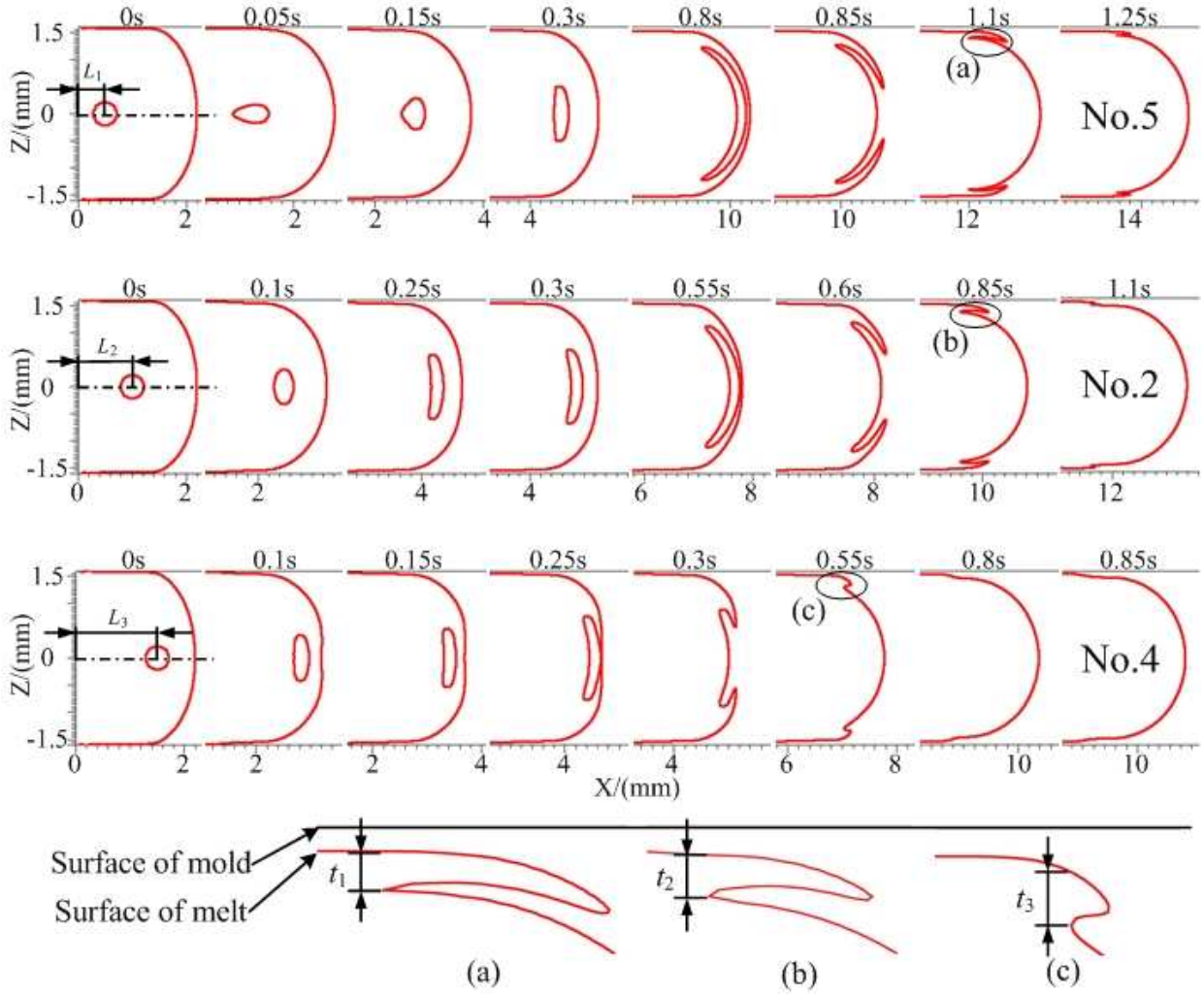

Figure 13 Morphological evolution of bubble in the front part of polymer melt obtained from simulation scheme 5, 2 and 4

Figure 14 compared the numerical simulation results of the polymer surface collapse depth for the different simulation scheme 5, 2 and 4 at the filling time of 1.7s. The curves in the figure represent the interface shapes of polymer surface for different cases. The D_1 - D_3 represent the maximum depth of the polymer melt surface collapse of the simulation scheme 5, 2 and 4, respectively. It can be seen that the relation of three collapse depths is $D_3 > D_2 > D_1$. Combining with figure 13, it can easily draw a conclusion that the shorter the distance from the initial bubble position to the flow front interface is, the thicker the bubble skin after its bursting is, the deeper the polymer surface collapse behind the bubble skin is. This is because that, in the melt filling process, the formed bubble skin turns into the obstacle of the rear melt, leads to the polymer surface behind the bubble skin not to maintain plane state, and finally makes the polymer surface separate from the mold wall and form a collapse defect. The thinner the bubble skin is, the smaller the impediment imposed on the rear melt is, and the shallower the surface collapse of plastic part is, vise versa.

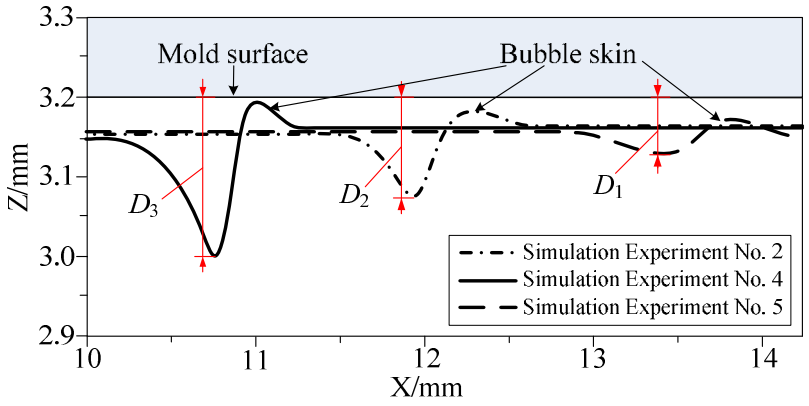

Figure 14 Comparison of polymer surface collapse depths of numerical simulation scheme 5, 2 and 4 at the filling time of 1.7s

5.3 Morphological Evolution of bubble deviating from the neutral plane of injection flow field

Figure 15 shows the morphological evolution of bubble with the initial position deviating from the neutral plane of melt flow field in the filling process of MFIM, which is corresponding to simulation scheme 7 (h=2.4mm, L=1mm, d=0.2mm). The upper part of figure 15(a)-(j) and (p)-(t) shows the temperature distribution of the polymer melt, and the lower part is the velocity (X directional) distribution diagram of the polymer melt. Figure 15(p)-(t) are the partially enlarged drawing of the back-end bubble skin, and figure 15(k)-(o) are the partially enlarged drawing of temperature distribution of the front-end bubble skin. Figure 15(a)-(f) show the deformation and bursting process of the bubble. Figure 15(g)-(i) show the formation process of surface defect of polymer. Table 7 shows the corresponding relation between figure icon, filling time and the maximum value of melt flow velocity.

As shown in figure 15(a)-(g), under the action of fountain flow, the bubble approaches to the flow front interface, and at the same time, deviates from the neutral plane. Then it is pushed to the mold cavity wall and finally burst on the mold surface. Figure 15(h)-(j) gives the formation of a surface pit and the evolution process of the front-end and back-end residual bubble skin after bubble bursting. It can be seen from figure 15(h) that, when the bubble is bursting, the bubble skins between the front-end and back-end of the pit have an obvious morphological difference, and with the progress of polymer melt filling the mold cavity, the evolution process of these two parts of bubble skin is obviously different too.

The morphology of bubble depends on the flow field environment in which it lies. As we can see from figure 15(a)-(g), in the initial stage of deformation, the bubble is located in the high temperature area where the flow ability of polymer melt is favorable. The bubble is easily pushed to mold cavity surface under the action of fountain flow. The back-end of the bubble gets close to the mold surface firstly, as shown in figure 15(e). At this moment, the melt around the back-end of bubble is gradually cooled down and its flow ability gradually decreases. As a result, the movement of the whole bubble, especially the back half part of the bubble, begins to slow down along the polymer filling direction. But the melt near the front-end of bubble has relatively strong flow ability and continues to flow along the filling direction since its temperature is still relatively high. As a result, the bubble is elongated into a slender shape, as shown in figure 15(e)-(g).

Figure 15(g) shows the moment of the bubble bursting after it touching the mold cavity wall. Interestingly, the bubble bursting position is not the bubble's back-end approaching to the mold cavity wall in the earliest, but the front-end. The reason is that the bubble's back-end is hard to touch the mold wall subject to the obstruction of polymer melt condensing layer, while the fluid ability of the melt near the bubble's front-end is better, the front-end can continuously approach to and finally touch the mold wall to burst. The two parts of bubble skin formed after bursting exhibit completely different evolution processes.

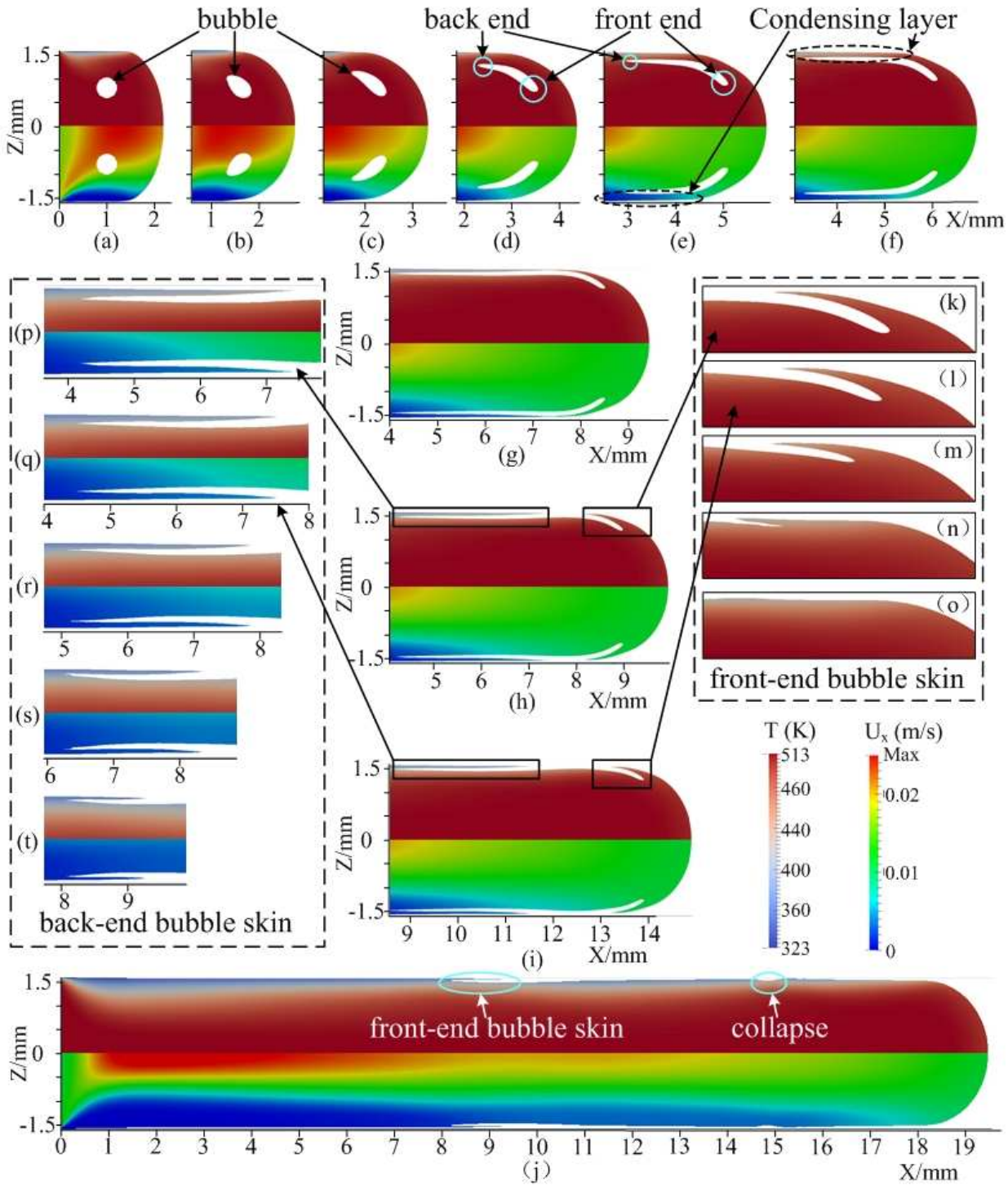

Figure 15 Morphological evolution of bubble obtained from the simulation scheme 7

Figure 15(k)-(o) give the evolution process of the front-end bubble skin. Since the temperature of melt surrounding it is high, the residual bubble skin is gradually swallowed and eventually disappears. Figure 15(p)-(t) give the evolution process of the back-end bubble skin. The temperature of melt surrounding it is low. The back-end bubble skin is relatively far away from the fountain flow field and hardly influenced by the fountain flow. Its location is not changed almost. But its shape renders as length decreasing, thickness thinning and decreasing of its gap with the internal melt.

As shown in figure 15(j), when the polymer filling time comes to the 1.7s, the collapse phenomenon is found

behind the front-end bubble skin on the surface of the plastic part, but the surface near the back-end bubble skin remains flat. This is because that the formation of collapse defects behind the bubble skin needs an appropriate temperatures range of the polymer melt. On one hand, if the temperature is too high, the polymer melt with strong fluid ability can quickly engulf the bubble skin and the engulfed bubble skin has a little influence on the rear melt surface. As a result, the rear melt surface collapse will not occur. The simulation result of the simulation scheme 1 shown in figure 12 is just this kind of circumstance. On the other hand, if the temperature is too low, the polymer melt surface will condensate quickly and its shape is hard to be changed, the surface collapse of the polymer melt behind the bubble skin will not appear, as shown in 15(p)-(t).

Table 7 Corresponding relations between figure icon, filling time and the maximum value of melt flow velocity

Figure icon	Time(s)	Max.U_x(m/s)
a	0	0.0154
b	0.05	0.0158
c	0.1	0.0165
d	0.2	0.0177
e	0.35	0.0192
f	0.45	0.020
g	0.7	0.0215
h	0.75	0.0218
i	0.85	0.0223
j	1.7	0.0254
k	0.75	/
l	0.85	/
m	1	/
n	1.2	/
o	1.7	/
p	0.75	0.0218
q	0.85	0.0223
r	1	0.023
s	1.2	0.0237
t	1.7	0.0254

5.4 Morphological Evolution of bubble with different initial diameters and positions deviating from the neutral plane of injection flow field

This section mainly studied the morphological evolution of bubble with different initial sizes and positions on the Z axis direction, that is, different initial positions of bubble deviating from the neutral surface of injection flow field. Figure 16 gives the simulation results of simulation scheme 6, 7 and 8 (h=2.4mm, L=1mm), where the bubble initial position is located on the section of thickness with the different initial diameters d_1=0.15mm, d_2=0.2mm, d_3=0.25mm. The X axis denotes the coordinate along the flow field direction, where the inlet is the origin of the coordinate. The Z axis denotes the distance to the neutral surface of flow field. Figure 16(a)-(c) respectively give the simulation results corresponding to simulation scheme 6, 7 and 8, where figure 16(d) shows the enlarged drawing of areas circled by the dotted rectangular box in figure 16(a)-(c).

From figure 16, it can be seen that the length of surface pits formed by the bubbles with different initial size is different, as shown as 8.1mm, 11.1mm and 12.2mm in figure 16(a)-16(c). With the increase of the initial diameter of

the bubble, the length of surface pits increases. What reasons make such length difference, obviously, the volume or size difference of the bubbles is not enough to cause such distinct length difference. From figure 16(a)-(c), it can be seen that the evolution of these three back-end bubble skin is almost the same, even after the long time of evolution, the morphology of three back-end bubble skins is also quite similar and their positions is basically fixed, as shown as a-2, b-2 and c-2 in figure 16(d). Nevertheless, the evolution of these three front-end bubble skins is quite different. The authors considered that this difference is caused by different bursting locations of bubbles.

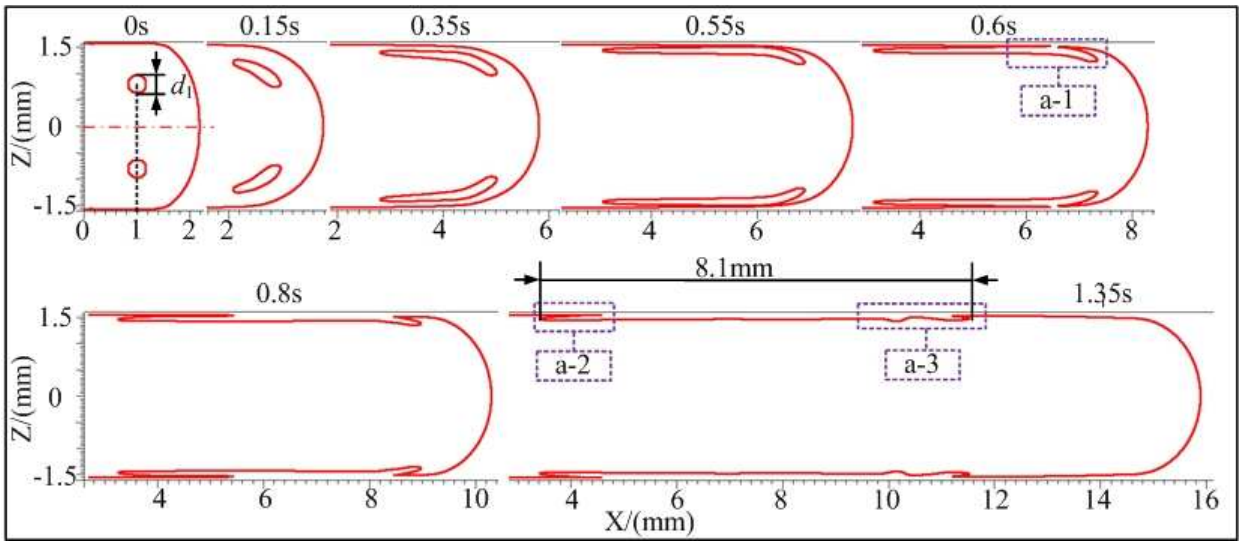

(a)

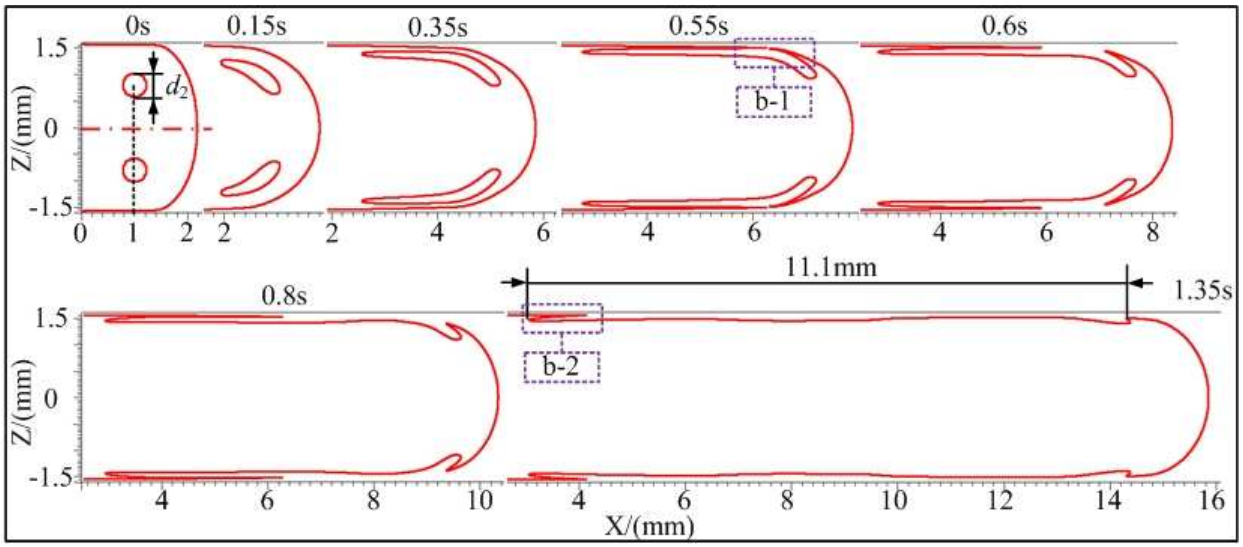

(b)

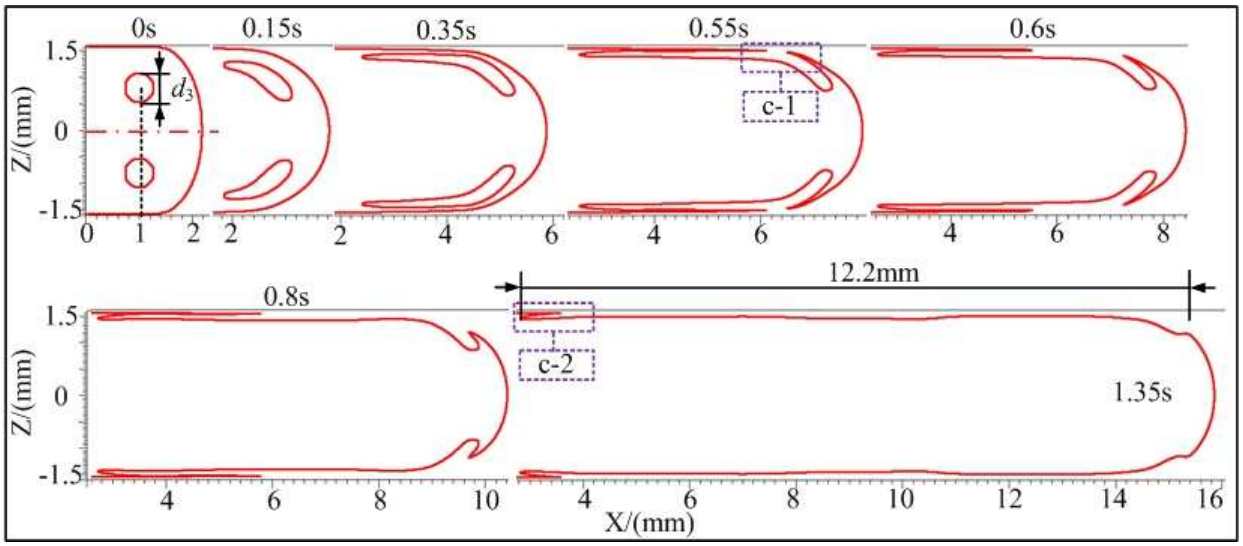

(c)

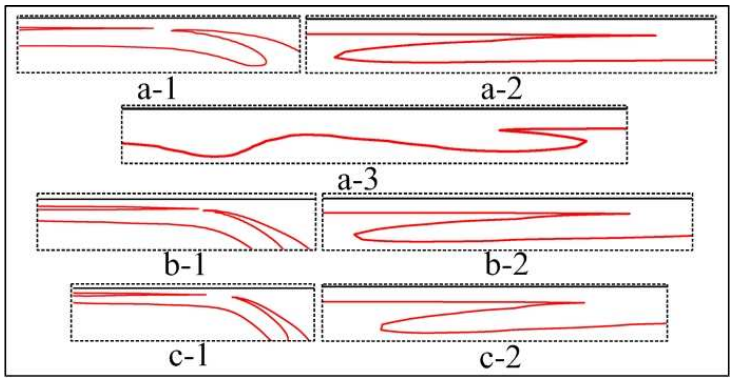

(d)

Figure 16 Morphological evolution of bubble obtained by simulation scheme 6, 7 and 8 (h =2.4mm, L =1mm). (a) simulation result of scheme 6, (b) simulation result of scheme 7, (c) simulation result of scheme 8, (d) partially enlarged drawing of simulation results

As shown in a-1, b-1 and c-1 of figure 16(d), for the bubble with the smallest initial diameter, when it bursts, the most part of the front-end bubble skin has touched the mold cavity wall. But, for the bubble with the largest initial diameter, when it bursts, the front-end bubble skin has not yet touched the mold cavity wall. The front-end skin of the bubble with a smallest size touches the mold cavity wall in a large area and is obviously subject to the cooling action from the mold. It is hard to disappear because it has the poorest fluid ability among the three bubble skins. In contrast, for the bubble with a big diameter, since the front-end bubble skin is located in the high temperature area of polymer melt with better flow ability, it almost disappears at the last moment of simulation, as shown in figure 16(b) and (c). For the bubble with a small diameter, the front-end bubble skin still remains at the last moment of simulation due to the skin in a low temperature area, as shown in figure 16(a). Therefore, this flow ability difference of different front-end bubble skins causes a large difference of displacement distance of front-end bubble skins in the polymer filling process.

In the formation process of pits, the back-end bubble skins is basically fixed but the front-end bubble skins continuously migrate forwards, and finally the pits is elongated significantly. According to this viewpoint, it can be concluded that the bursting location of the bubbles is the main factor influencing the length of the pit. The bubble bursting on the triple point of polymer melt, mold and air easily leads to a longer pit, and actually, this kind of long pit is the silver mark defect on the surface of MFIM parts. While the bubble bursting on the mold surface produces a shorter pit or an unobvious silver mark defect.

From a-3 shown in figure 16(d), it can be also seen that the collapse phenomenon appears behind the front-end bubble skin on the polymer surface, but it is not found near the back-end bubble skin. This is because that the bubble skin works as barrier to the subsequent polymer melt in the flow process, and the melt surface with high flow ability is difficult to keep the plane state. From a-3 in figure 16(d), it can be also found that the rear area of front-end bubble skin is bottom of the pit which has not touched the mold surface. This area has a good flow ability and can easily form the collapse phenomenon. But the polymer melt near the back-end bubble skin has been cooled down and its flow ability becomes poor. Thus it is hard to form the collapse phenomenon.

To further reveal the morphological evolution of the pit caused by the bubble bursting on the mold cavity surface, figure 17 gives the corresponding numerical simulation results. Figure 17(a) shows the flow front and the viewing angle of bubble. Figure 17(b) provides the partially enlarged drawing of figure 7(a) with the camera site located behind the flow front to display the real morphology of the pit on the plastic part surface. Figure 17(c) is the numerical simulation result of the bubble bursting process and the morphological evolution of pit on the mold cavity surface obtained by the mathematical model established in this paper.

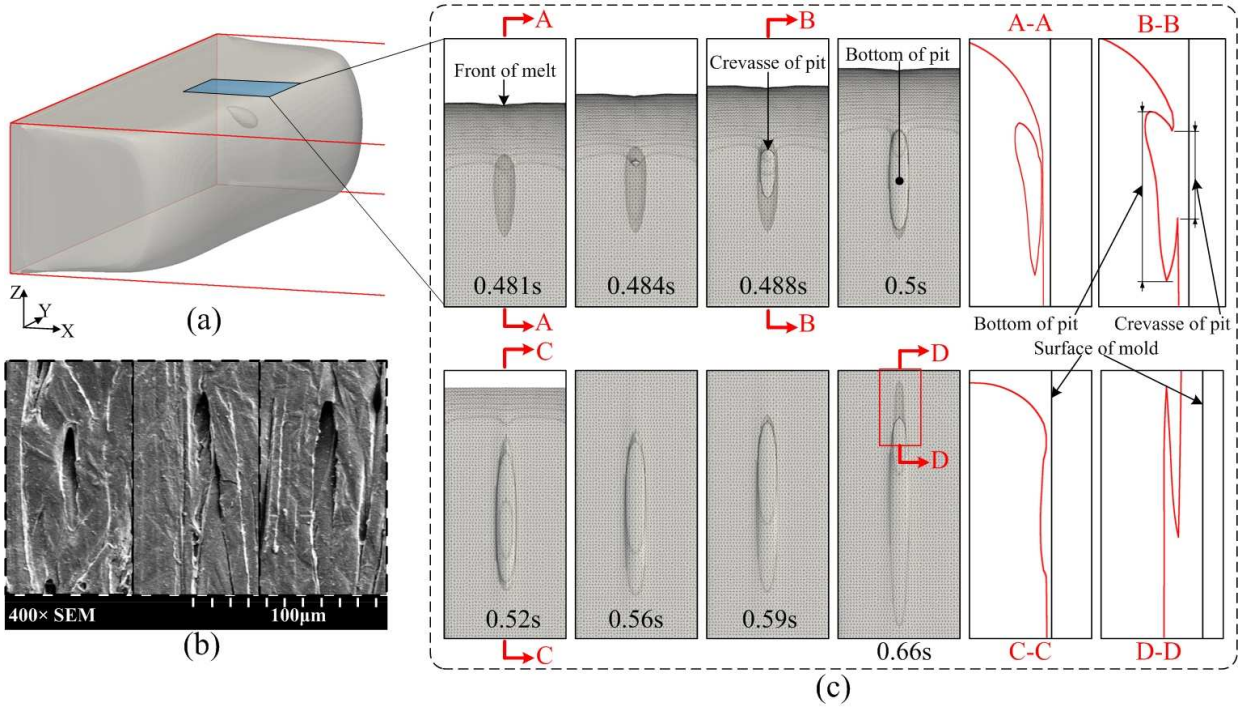

Figure 17 Morphological evolution of the pit caused by the bubble bursting on the mold cavity surface. (a) the flow front and the viewing angle of bubble, (c) SEM of pit, (d) numerical simulation result of the bubble bursting process and morphological evolution of pit

From figure 17, we can see that the bubble has not been formed into a slender shape before bursting, as shown in A-A section in figure 17(c). After bubble bursting, the residual bubble skin quickly touches the mold wall surface. As stated above, this early contact of the skin with the mold wall surface leads to decline of the flow ability of bubble skin, and a relatively short pit is caused finally, as shown in figure 17(b). The morphology of bubble when it happens to burst determines the subsequent evolution of pit. Form the B-B section of the figure 17(c), it can be seen that there is a distance between the pit bottom and mold cavity wall, and the pit depth changes from shallow to deep along the polymer filling direction. In the following-up evolution process, the pit bottom extends to underneath of the front polymer, as shown in D-D section of figure 17(c).

According to the simulation results, the reason causing this kind of pit morphology lies in the flow ability difference between the bottom and the crevasse of pit. In comparison with the pit crevasse cooled by mold cavity wall, the pit bottom is not subject to the cooling influence of mold cavity wall and thereby has a better flow ability. This

difference results in a relative displacement between the pit crevasse and bottom. At last, the pit morphology with deep front and shallow rear is finally formed, as shown in figure 17(b). Through the above comparison and analysis, it can be seen that the simulation results about the position and morphology of pit are in good agreement with those of the short shot experiment.

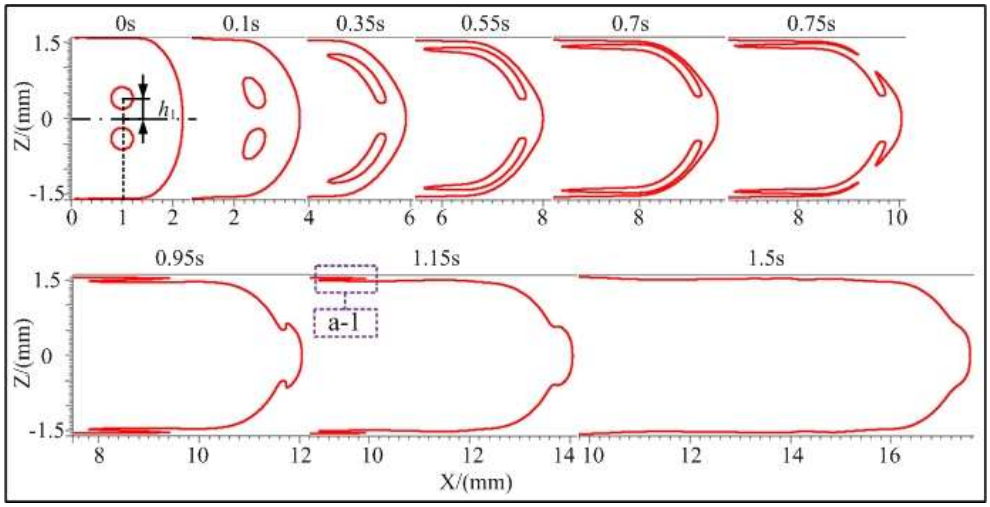

(a)

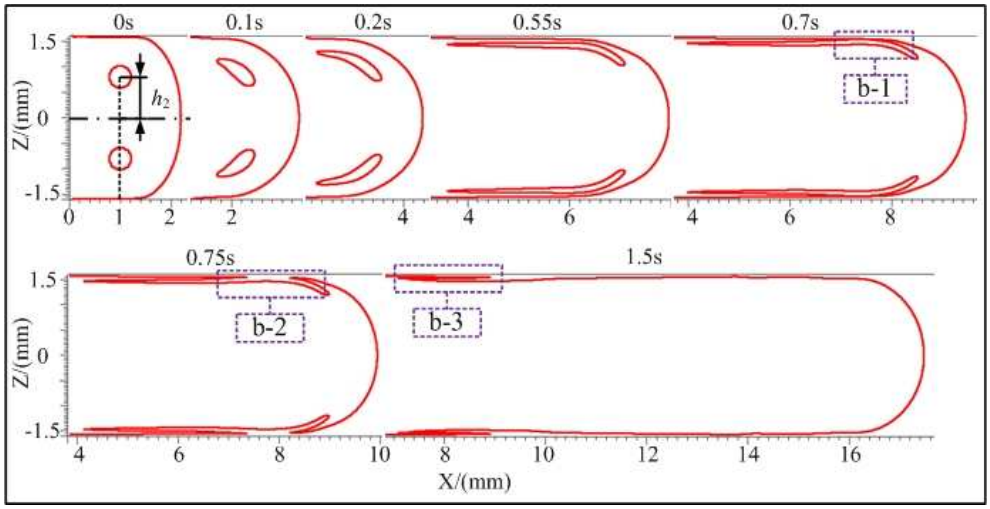

(b)

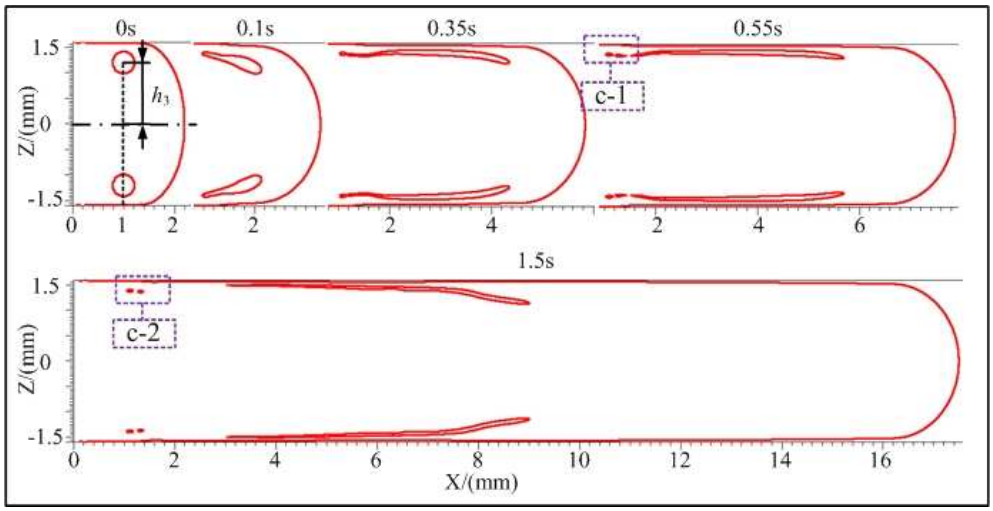

(c)

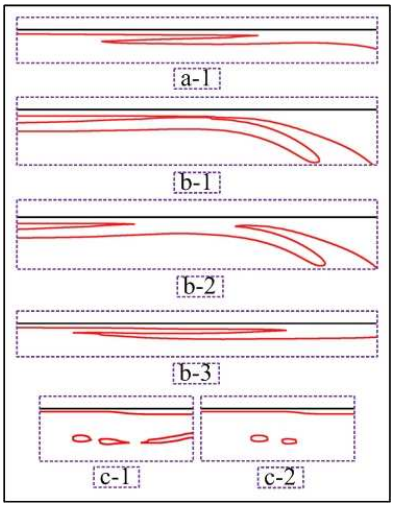

(d)

Figure 18 Morphological evolution of bubble obtained from simulation scheme 9, 7 and 10. (a) result of scheme 9, (b) result of scheme 7, (c) result of scheme 10, (d) partially enlarged drawing of simulation results

Figure 18 shows the morphological evolution of the initial bubble deviating from the neutral plane of injection flow field with three distances (h_1=0.4mm, h_2=0.8mm, h_3=0.12mm), which respectively correspond to simulation scheme 9, 7 and 10 listed in the table 4. From figure 18, the firstly bursting bubble is neither the bubble whose initial position is closest to the polymer surface, as shown in figure 18(c), nor the bubble whose initial position is farthest from the polymer surface, as shown in figure 18(a), but the bubble whose initial position is located in the middle, as shown in figure 18(b). This is because that the migration of bubble interface is hampered by the polymer condensation layer and not subjected to squeezing action of fountain flow, as shown in figure 18(c). As a result, the bubble is difficult to reach the mold cavity surface and burst. But if the temperature of polymer melt surrounding the bubble is high, this kind of elongated bubble is still possible to burst. This paper has not yet studied the effect of the mold cavity surface temperature on the bubble deformation, bursting behavior and bubble skin evolution process. This effect is still worthy to study in the future.

As shown in figure 18(c), the slender bubble is further stretched by polymer melt in the filling direction and the back end of bubble is finally separated into two small bubbles. c-1 and c-2 in figure 18(d) give the enlarged drawing of these two bubbles. The front-end of bubble begins to extend to the flow field center under the action of injection flow field, as shown in the elliptical wireframe of figure 18(c). Figure 19 gives the temperature field, velocity field and hodograph of flow field at the filling time of 1.5s for simulation scheme 10. It can be surmised that there is a velocity component pointing to the neutral surface of the velocity field around the bubble front-end interface. This velocity component leads to the front-end of bubble extending to the center of the flow field.

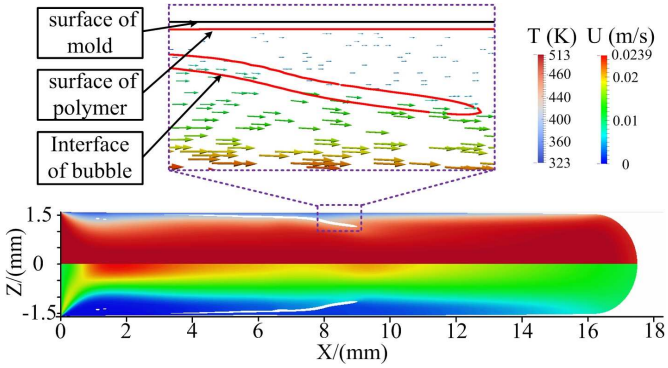

Figure 19 Temperature field, velocity field and hodograph of flow field at filling time of 1.5s for simulation scheme 10

6、Conclusion

This paper established an incompressible, unsteady, non-isothermal 3D mathematical model of multiphase flow in MFIM process. A new set of boundary conditions and its applying method were proposed. The energy equation was coupled into the PIMPLE loop algorithm and the temperature divergence problem on the interface between two phases with large viscosity ratio was effectively overcome. The tracking accuracy of micron grade bubbles interface in macroscopic scale flow field was improved significantly by using physical field variables based AMR technology. With the established mathematical model and MFIM short shot experiment of flexural sample, the bubble morphological evolution in the filling process of MFIM was obtained. The following conclusions were drawn:

1. The established model successfully predicted the surface collapse phenomenon near the pit formed by bubble bursting, and the existence of the collapse was verified in the SEM photo of plastic part surface. This collapse could only appear in a certain range of polymer melt temperature, and the barrier action of the bubble skin to polymer melt flow is the main reason of causing this collapse.

2. The formation mechanism of the pit with deep front and shallow rear on the plastic part surface was revealed. This kind of pit is formed only when a bubble bursts on the mold cavity wall. It is the flow ability difference of polymer melt in the bottom and the crevasse of pit to cause this kind of pit with deep front and shallow rear.

3. The morphological evolution of bubble before bursting can be divided into two cases according to the bubble initial position, the bubble on the neutral surface of flow field and the bubble deviating from the neutral surface of flow field. The former experiences the morphological evolution of circle, oval, crescent, and continuously approaching to the flow front. The later experiences the morphological evolution of circle, teardrop, slender, and continuously approaching to the mold cavity wall. Nevertheless, in melt filling process, it is not always true that the closer to the mold cavity wall the bubble is, the more easily the bubble burst. Once the polymer condensation layer is formed, it will hamper the bubbles approaching to mold cavity wall. Without the transport of fountain flow and a relatively high temperature of polymer melt, the bubbles are hard to reach the mold cavity wall to burst.

4. The morphological evolution of bubble after bursting can be divided into three cases according to the bubble bursting position: (1) bubble bursting on the interface between melt and air, i.e., the flow front, (2) bubble bursting on the interface between melt and mold, i.e., the mold wall, (3) bubble bursting on the triple point of polymer melt, mold and air. In the first case, the residual skins formed after bursting of the bubbles with small initial size or those whose nucleation position is close to flow front can completely disappear before touching mold cavity wall without any dreadful effect on the product surface quality. In the second case, the burst bubble is affected by the cooling effect of mold cavity wall, and it is not easy to be stretched and form a thin silver defect but a pit with deep front and shallow rear. In the third case, the burst bubbles most likely result in the silver mark defects. This is because that there exists a flow ability difference between front-end bubble skin and back-end bubble skin after bubble bursting, and the pit is elongated and silver mark morphology is formed.

5. The comparison of numerical simulation results with those of short shot experiment indicated that the model established in this paper can accurately capture the phase interface of multiphase in the 3D flow field and simulate the overall process of bubble morphological evolution in the filling process of MFIM. By using this model, we can get the bubble bursting and disappearing process which is hard to be caught with the visual equipment. Furthermore, the boundary conditions and their applying method provide a reliable guarantee for accurate description of the bubble morphological evolution in the filling process of the MFIM.

Acknowledgements

This research work was supported by Program for Chang Jiang Scholars and Innovative Research Team in University of Ministry of Education of China (No. IRT0931), Research Award Fund for Shandong Province Excellent Innovation Team (No. 2012-136).

References

[1] J. E. Martini. Master's Thesis, University of Massachusetts, 1981.

[2] J. E. Martini, F. A. Waldman and N. P. Suh, *SPEANTEC Tech Papers*, 1982, 28: 674-676.

[3] J. Y. Xu, *Microcellular Injection Molding*, ed. R. F. Grossman and D. Nwabunma, John Wiley & Sons, 2011, vol. 9, ch.1, pp. 1-11.

[4] A. Kramschuster, L. S. Turng and J. Biomed, *Mater. Res. B.*, 2010, 92: 366-376.

[5] H. Y. Mi, X. J. Max, R. Salick, L. S. Turng and X. F. Peng, *J. Mater. Res.*, 2014, 29(8): 911-922.

[6] G. L. Wang, G. Q. Zhao, J. C. Wang and L Zhang, *Polym. Eng. Sci.*, 2014, 55: 807–835.

[7] G. W. Dong, G. Q. Zhao, Y. J. Guan, G. L. Wang and X. X. Wang, *J. Appl. Polym. Sci.*, 2014, DOI: 10.1002/app.40365.

[8] S. Li, G. Q. Zhao, G. L. Wang, Y. J. Guan and X. X. Wang, *J. Cell. Plast.*, 2014, 50(5): 415-435.

[9] J. J. Lee, L. S. Turng, E. Dougherty and P. Gorton, *Polym.*, 2011, 52: 1436-1446.

[10] S. W. Cha and J. D. Yoon. *Polym-Plast. Technol.*, 2005, 44(5): 795-803.

[11] *US Pat.*, 6 884 823, 2005.

[12] A. N. J. Spoerrer, D. S. Bangarusampath and V. Altstaedt, *Cell. Polym.*, 2008, 27(2): 101-121.

[13] S. C. Chen, W. H. Liao and R. D. Chien, *Int. Commun. Heat. Mass.*, 2012, 39(8): 1125-1131.

[14] S. C. Chen, P. S. Hsu and S. S. Hwang, *J. Appl. Polym. Sci.*, 2013, 127(6): 4769-4776.

[15] C. D. Han and H. Yang, *J. Appl. Polym. Sci.*, 1984, 29(12): 4465-4470.

[16] J. Colton and N. Suh, *Polym. Eng. Sci.*, 1987, 27(7): 485-492.

[17] N. S. Ramesh, G. A. Campbell and D. H. Rasmussen, *Polym. Eng. Sci.*, 1994, 34(22): 1685-1697.

[18] C. D. Han and H. J. Yoo, *Polym. Eng. Sci.*, 1981, 21(9): 518-533.

[19] M. Amon and C. D. Denson, *Polym. Eng. Sci.*, 1984, 24(13): 1026-1034.

[20] A. Arefmanesh, S.G. Advani and E. E. Michaelides, *Polym. Eng. Sci.*, 1990, 30(20): 1330-1337.

[21] N. S. Ramesh, D. H. Rasmussen and G. A. Campbell, *Polym. Eng. Sci.*, 31(23): 1657-1664.

[22] A. Osorio and L. S. Turng, *Polym. Eng. Sci.*, 2004, 44(12): 2274-2287.

[23] S. N. Leung, C. B. Park, D. L. Xu, H. B. Li and R. G. Fenton, *Ind. Eng. Chem. Res.*, 2006, 45(23): 7823-7831.

[24] C. A. Villamizar and C. D Han, *Polym. Eng. Sci.*, 1978, 18(9): 699-710.

[25] C. D. Han and H. J. Yoo, *Polym. Eng. Sci.*, 1981, 21(9): 518-533.

[26] M. Mahmoodi, A. H. Behravesh, S. A. M. Rezavand and A. Pashaei, *J. Appl. Polym. Sci.*, 2010, 116(6): 3346-3355.

[27] A. Wong and C. B. Park, *Polym. Test.*, 2012, 31(3): 417-424.

[28] A. Ahmadzai, A. H. Behravesh, M. T. Sarabi and P. Shahi, *J. Cell. Plast.*, 2014, 50(3): 279-300.

[29] S. B. Pillapakkam and P. Singh, *J. Comput. Phys.*, 2001, 174(2): 552-578.

[30] I. B. Bazhlekov, P. D. Anderson and E. H. M. Han, *J. Colloid. Interf. Sci.*, 2006, 298(1): 369-394.

[31] P. Yue, J. J. Feng, C. Liu and J. Shen, *J. Fluid. Mech.*, 2005, 540: 427-437.

[32] J. Lee and C. Pozrikidis, *Comput. & fluid.*, 2006, 35(1): 43-60.

[33] P. J. A. Janssen and P. D. Anderson, *Phys. Fluid.*, 2007, 19(4): 043602.

[34] A. M. Ardekani, S. Dabiri and R. H. Rangel, *Phys. Fluid.*, 2009, 21(9): 093302.

[35] K. Verhulst, R. Cardinaels, P. Moldenaers, S. Afkhami and Y. Renardy, *J. Non-newton. Fluid.*, 2009, 156(1): 44-57.

[36] S. S. Rabha and V. V. Buwa, *Chem. Eng. Sci.*, 2010, 65(1): 527-537.

[37] Y. K. Wei, Y. Qian and H. Xu, *J. Comput. Multip. Flow.*, 2012, 4(1): 111-118.

[38] H. Park, R. B. Thompson, N. Lanson, C. Tzoganakis, C. B. Park and P. Chen, *J. Phys. Chem. B.*, 2007, 111(15): 3859-3868.

[39] M. Lee, C. B. Park and C. Tzoganakis, *Polym. Eng. Sci.*, 1999, 39(1): 99-109.

[40] W. Huang and R. D. Russell, *Adaptive moving mesh methods*. ed. S.S Antman, J.E. Marsden and L. Sirovich. Springer, New York, 2011.
[41] H.G. Weller, G. Tabor, H. Jasak, and C. Fureby, *Comput. Phys.*, 1998, 12(6):620-631.
[42] C. W. Hirt and B. D. Nichols, *J. Comput. Phys.*, 1981, 39(1): 201-225.
[43] S. O. Unverdi and G. Tryggvason, *J. Comput. Phys.*, 1992, 100(1): 25-37.
[44] W. Martin, *Microfluid. Nanofluid.*, 2012, 12(6): 841-886.
[45] J. U. Brackbill, D. B. Kothe and C. Zemach, *J. Comput. Phys.*, 1992, 100(2): 335-354.
[46] H. E. Park and J. M. Dealy, *Macromolecules*, 2006, 39(16): 5438-5452.
[47] D. Raps, T. Köppl, De Anda AR and V. Altstädt, *Polym.*, 2014, 55(6): 1537-1545.
[48] H. Fujita and A. Kishimoto, *J. Polym. Sci.*, 1958, 28(118): 547-567.
[49] J. R. Royer, J. M. D. Simone and S. A. Khan, *J. Polym. Sci. B.*, 2001, 39(23): 3055-3066.
[50] J. F. Hetu, D. M. Gao, A. Garcia-Rejon and G. Salloum, *Polym. Eng. Sci.*, 1998, 38(2): 223-236.
[51] OpenFOAM, http://www.openfoam.com/, (accessed October 2014)
[52] J. A. Horacio, M. D. Santiago, M. J. Gimeneza and M. N. Norberto, *Mechan. Comput.*, 2013, 32:995-1011.
[53] P. Yue, C. Zhou, J. J. Feng, C. F. Ollivier-Gooch and H. H. Hu, *J. Comput. Phys.*, 2006, 219(1): 47-67.
[54] I. Ginzburg and G. Wittum, *J. Comput. Phys.*, 2001, 166(2): 302-335.
[55] H. J. Yoo and C. D. Han, *Polym. Eng. Sci.*, 1981, 21(2): 69-75.
[56] H. J. Yoo and C. D. Han, *J. Rheol.*, 1981, 25(1): 115-137.
[57] G. I. Taylor, *P. Roy. Soc. A-math. Phy.*, 1934: 501-523.